

**Manuscript Title:** The cytosolic domain of T-cell receptor  $\zeta$  associates with membranes in a dynamic equilibrium and deeply penetrates the bilayer

**Manuscript No:** JBC/2017/794370 [R1]

**Manuscript Type:** Regular Paper

**Date Submitted by the Author:** 18 Aug 2017

**Complete List of Authors:** Kerstin Zimmermann, Rebecca Eells, Frank Heinrich, Stefanie Rintoul, Brian Josey, Prabhanshu Shekhar, Mathias Lösche, and Lawrence J Stern

**Keywords:** membrane bilayer; neutron scattering; protein phosphorylation; signal transduction ; T-cell receptor (TCR); dynamic equilibrium; neutron reflectometry ; protein/membrane interaction

The cytosolic domain of T-cell receptor  $\zeta$  associates with membranes in a dynamic equilibrium and deeply penetrates the bilayer

**Kerstin Zimmermann, Rebecca Eells, Frank Heinrich, Stefanie Rintoul, Brian Josey, Prabhanshu Shekhar, Mathias Lösche, Lawrence J Stern**

From the Department of Pathology, University of Massachusetts Medical School, Worcester MA 01655

Department of Physics and Department of Biomedical Engineering, Carnegie Mellon University, Pittsburgh PA 15213

NIST Center for Neutron Research, 100 Bureau Drive, Gaithersburg MD 20899

To whom correspondence should be addressed: Prof. Lawrence J. Stern, Department of Pathology, University of Massachusetts Medical School, 55 Lake Avenue North, Worcester, MA 01655  
Telephone: (508) 856-1831; FAX: (508) 856-0019; E-mail: Lawrence.Stern@umassmed.edu

Running Title: *TCR $\zeta_{\text{cyt}}$  membrane association*

Keywords: T cell receptor signaling, neutron reflectometry protein/membrane-interaction, phosphorylation, dynamic equilibrium

## ABSTRACT

Interactions between lipid bilayers and the membrane-proximal regions of membrane-associated proteins play important roles in regulating membrane protein structure and function. The T-cell antigen receptor (TCR) is an assembly of eight single-pass membrane-spanning subunits on the surface of T-lymphocytes that initiates cytosolic signaling cascades upon binding antigens presented by MHC-family proteins on antigen-presenting cells. Its  $\zeta$  subunit contains multiple cytosolic immunoreceptor tyrosine-based activation motifs (ITAMs) involved in signal transduction, and this subunit by itself is sufficient to couple extracellular stimuli to intracellular signaling events. Interactions of the cytosolic domain of  $\zeta$  ( $\zeta_{\text{cyt}}$ ) with acidic lipids have been implicated in the initiation and regulation of transmembrane signaling.  $\zeta_{\text{cyt}}$  is unstructured in solution. Interaction

with acidic phospholipids induces structure, but its disposition when bound to lipid bilayers is controversial. Here, using surface plasmon resonance and neutron reflection, we characterized the interaction of  $\zeta_{\text{cyt}}$  with planar lipid bilayers containing mixtures of acidic and neutral lipids. We observed two binding modes of  $\zeta_{\text{cyt}}$  to the bilayers in dynamic equilibrium: one in which  $\zeta_{\text{cyt}}$  is peripherally associated with lipid headgroups and one in which it penetrates deeply into the bilayer. Such an equilibrium between the peripherally bound and embedded forms of  $\zeta_{\text{cyt}}$  apparently control accessibility of the ITAMs to tyrosine kinases and may regulate the TCR signal transduction pathway. Our results reconcile conflicting findings of the  $\zeta$  structure reported in previous studies and provide a framework for understanding how lipid interactions regulate biological activities for this cell-surface receptor system.

The T-cell antigen receptor (TCR) is a multi-subunit cell-surface protein complex composed of eight single-pass transmembrane subunits arranged in pairs as  $(\alpha\beta)(\gamma\epsilon)(\delta\epsilon)(\zeta_2)$  (Fig. 1). The  $\gamma\epsilon$  and  $\delta\epsilon$  subunits carry the CD3 cell-surface epitope and are referred to by this name. (The ho-

modimeric  $\zeta_2$  subunit carries the CD247 epitope but is not usually referred to by using this designation.) TCR signal transduction is triggered by interaction with major histocompatibility (MHC)-peptide complexes on antigen-presenting cells. Variable and hypervariable regions on the extra-

cellular antigen-binding domains of the TCR  $\alpha\beta$  subunits contain the binding site for MHC-peptide. CD3 $\gamma$ ,  $\delta$ , and  $\epsilon$  possess extracellular immunoglobulin-like domains that form heterodimers and associate with TCR $\alpha\beta$ . The  $\zeta_2$  subunits have very small extracellular portions and associate with the receptor complex primarily via transmembrane interactions. The activation mechanism is incompletely understood at the molecular level, but it is well established that extracellular MHC-peptide binding triggers cytosolic signaling pathways (1), with the first step believed to be phosphorylation, by Src-family kinases, of tyrosine residues on intracellular TCR immunoreceptor tyrosine-based activation motifs (ITAMs) of the general sequence, YxxL/Ix<sub>(6-8)</sub>YxxL/I (2). The cytosolic domains of CD3 $\gamma$ ,  $\delta$ , and  $\epsilon$  each contain one ITAM, and the cytosolic domain of  $\zeta$  (TCR $\zeta_{\text{cyt}}$ ) has three.  $\zeta_{\text{cyt}}$  by itself can initiate signal transduction processes, as shown with chimeric proteins on which  $\zeta_{\text{cyt}}$  was fused to an unrelated extracellular domain (3) and used as a basis for chimeric antigen receptor (CAR) cancer immunotherapy (4).

A schematic representation of the intact TCR( $\alpha\beta$ )( $\gamma\epsilon$ )( $\delta\epsilon$ )( $\zeta_2$ ) complex is depicted in Fig. 1, but its three-dimensional structure is unknown. However, structures have been determined for several sections (5–13), such as the isolated TCR $\alpha\beta$  extracellular antigen-binding domains, both free (5) and MHC-bound (6). Structures of the extracellular domains of CD3 $\gamma\epsilon$  (7, 8) and CD3 $\delta\epsilon$  (8, 9) heterodimers were determined by NMR and X-ray crystallography, and recent small angle X-ray scattering, EM and NMR studies suggested their orientations relative to each other in the TCR complex. These studies showed consistently that the extracellular CD3 domains are located underneath the TCR $\alpha\beta$  chains (10–12), but disagreed on proposed docking sites of the CD3 subunits to TCR $\alpha\beta$  (11, 12). While the conformation of the small extracellular portion (9 residues) of  $\zeta$  is not known, the association of the helical transmembrane segments of  $\zeta_2$  in micelles was determined by NMR (13) and refined in molecular dynamics (MD) simulations within a lipid bilayer (14, 15). A model for the assembly of all eight transmembrane domains in the intact TCR complex has been proposed based on charge-pairing interactions within the bilayer (16). Finally, a recent study observed that cytosolic juxtamembrane regions of the two  $\zeta$ -subunits are divaricated in the TCR/CD3-complex but become juxtaposed upon TCR engagement (17).

CD3 $\gamma$ ,  $\delta$ ,  $\epsilon$  and TCR $\zeta$  each have substantial cytosolic domains with 45, 45, 55 and 113 residues, respectively, that are unstructured in solution (18–20). The isolated cytosolic domains of  $\zeta$  (19, 20) and CD3 $\epsilon$  (20, 21) – but not those of CD3 $\gamma$  and  $\delta$  (20) – bind to acidic lipids in lipid-detergent micelles (22), bicelles (21) and lipid vesicles (19, 20, 23) even in the absence of their transmembrane anchors. While  $\zeta_{\text{cyt}}$  is unstructured in solution as shown by CD, NMR, and fluorescence assays (18, 19, 22, 24), it interacts with lipid vesicles or lipid-detergent micelles for some (19, 20, 22) but not all (23) lipid compositions, depending on lipid acidity, and such interactions induce helical structure in the peptide and can destabilize or fuse vesicles (23). Cationic clusters on CD3 $\epsilon_{\text{cyt}}$  and  $\zeta_{\text{cyt}}$  have been identified that are critical for membrane binding (21, 23, 25–27) and, thereby, the regulation of signaling processes, as binding may sequester key residues in the membrane where they are inaccessible to cytosolic kinases and other signaling components (19, 21, 27). For example, an NMR structure of CD3 $\epsilon_{\text{cyt}}$  bound to POPG/DHPC bicelles showed that the protein is peripherally bound with its ITAM tyrosine residues buried within the hydrophobic membrane interior (21).

In vivo,  $\zeta_{\text{cyt}}$  binds to the inner plasma membrane as observed with FRET for chimeric protein in which the peptide was fused to the transmembrane and extracellular regions of CD2 or KIR2DL3 (irrelevant proteins in the context of MHC-TCR signaling) (25, 28). The cytosolic domain of TCR $\zeta$  by itself is thus sufficient to transduce activation signals across the cell membrane (3, 29–31) and has been a focus of studies of the molecular basis of T cell signaling (25, 32). However, the disposition of  $\zeta_{\text{cyt}}$  in the membrane and its implications for kinase accessibility remain unknown. In this study, we use a planar bilayer model, the sparsely-tethered lipid bilayer membrane (stBLM) (33), to investigate the membrane association of isolated  $\zeta_{\text{cyt}}$  in thermodynamic and structural terms by surface-plasmon resonance (SPR) and neutron reflectometry (NR), respectively. Molecular models based on these results visualize the localization of  $\zeta_{\text{cyt}}$  relative to the membrane. A phosphorylation assay based upon recombinant Lck tyrosine kinase was used to study the sequestering of ITAM tyrosines within the bilayer. Taken together, these results show conclusively that the interaction of the  $\zeta_{\text{cyt}}$  with the bilayer controls ac-

cessibility of signaling components and thus regu-

## RESULTS

### *Quantification of $\zeta_{\text{cyt}}$ membrane binding by SPR*

In the stBLM sample format (Fig. 2), a phospholipid bilayer is tethered to an Si-supported, atomically flat gold film via synthetic lipid anchors (34) that are spaced out by co-adsorption with  $\beta$ ME and thus passivate the solid substrate, provide a hydrated sub-membrane space, and allow for native-like interaction of membrane proteins (33). Bilayers were of various compositions, either zwitterionic (pure POPC) or acidic (POPC:POPG = 60:40 or POPC:POPS = 70:30), or with cholesterol (DOPC/DOPS/cholesterol = 65:35:3), and bathed in HEPES buffer (20 mM, pH 7.4) at high and low ionic strength (25 or 150 mM NaCl). POPG in binary bilayers was investigated for comparison with previous vesicle adsorption studies (19, 20). On the other hand, POPC:POPS = 70:30 provides a better representation of the inner cell membrane leaflet. Time-dependent SPR responses to  $\zeta_{\text{cyt}}$  incubation of such stBLMs were recorded for protein concentrations between 0.05  $\mu\text{M}$  and  $\approx 23 \mu\text{M}$ . SPR measurements were performed at 25.0  $^{\circ}\text{C}$ . While the bilayer membranes are in the fluid phase at 25.0  $^{\circ}\text{C}$  as they would be at physiological temperature, the entropic barrier to binding is slightly higher at physiological temperatures. Therefore, apparent binding constants observed under our experimental conditions would be expected to be somewhat reduced but the general behavior of the protein is not expected to be qualitatively different.

Figure 3 shows representative SPR data. Binding of  $\zeta_{\text{cyt}}$  to pure POPC stBLMs was insignificant, even at 25 mM NaCl where electrostatic interactions are minimally shielded (Fig. 3A). Binding of  $\zeta_{\text{cyt}}$  to POPG-containing membranes (POPC/POPG 60:40) leads to a fast increase of the SPR signal after each injection, followed by an approximately exponential decay of the signal to a new baseline above that of the previous, lower concentration (Fig. 3B). This indicates that protein binds to the membrane in two distinct modes – an initial fast association followed by a slow process that does not reach equilibration during the time course of the experiment. Extrapolated SPR response values,  $R_{\infty}$ , at the end of each incubation are well described by a Langmuir binding model with dissociation constant,  $K_d = 4.0 \pm 1.4 \mu\text{M}$  ( $n = 2$  measurements). SPR traces for the binding of  $\zeta_{\text{cyt}}$

lates an intermediate stage of signal transduction.

to POPS-containing stBLMs (POPC/POPS 70:30) showed a similar response (Fig. 3C), with a dissociation constant of  $K_d = 5.4 \pm 2.2 \mu\text{M}$  ( $n = 3$ ). Adding cholesterol to a DOPC/DOPS membrane composition (DOPC/DOPS/cholesterol 65:35:3), does not substantially alter either the observed binding behavior (Fig. 3D) or the apparent binding constant. The DOPC/DOPS/cholesterol data are best fit by a Langmuir binding model with  $K_D = 4.3 \pm 0.2 \mu\text{M}$  (Fig. 3D), which is comparable to those measured for POPC/POPG and DOPC/DOPS membranes. At 150 mM NaCl, binding of  $\zeta_{\text{cyt}}$  to POPS-containing stBLMs is strongly reduced (Fig. 3E). Here, binding kinetics were considerably slowed down and low concentrations of  $\zeta_{\text{cyt}}$  caused small decreases of the SPR response, and increases in SPR signal were only observed at high  $\zeta_{\text{cyt}}$  concentrations ( $> 6.7 \mu\text{M}$ ,  $n = 3$ ), yielding an estimated dissociation constant,  $K_d > 25 \mu\text{M}$ .

### *Bilayer integrity*

In the light of a previous report that  $\zeta_{\text{cyt}}$  may disrupt vesicles upon incubation (23), we monitored the integrity of bilayers in contact with the protein. Negative-stain transmission EM showed that POPC:POPG (60:40, total lipid: 3 mM) vesicles were not affected in their morphology by 10  $\mu\text{M}$   $\zeta_{\text{cyt}}$  (data not shown). In addition, the hydrodynamic radii of these vesicles without and with 5  $\mu\text{M}$  protein were indistinguishable, as reported by dynamic light scattering. As a more sensitive probe of membrane integrity we used Electrical Impedance Spectroscopy (EIS), which measures dielectric (insulating) properties and is a sensitive readout of bilayer quality in stBLMs (33). The EIS response has been modeled using an equivalent circuit yielding the capacitance of the intact membrane and the conductance and capacitance of parallel conductive pathways induced by protein interaction (33). Using this approach, we monitored the EIS signatures of POPC:POPS (70:30) bilayers prior to and after completion of an SPR experiment at which maximum surface coverage has been achieved (Fig. 4). We typically observed an increase in membrane conductance that was less than 5  $\mu\text{S cm}^{-2}$ . For comparison, the introduction of a pore-forming toxin like  $\alpha$ -hemolysin would lead to an increase of the membrane conductance of over 100  $\mu\text{S cm}^{-2}$  well below saturation surface coverage (35). We therefore conclude that our

studies of  $\zeta_{\text{cyt}}$  on stBLMs report protein interaction with intact membranes.

### *Structural characterization of membrane-bound $\zeta_{\text{cyt}}$*

Neutron reflection (NR) is a well-established technique to determine interfacial structure in the normal direction of supported planar bilayers as time and ensemble averages of molecular conformations within the plane of the sample (36). Changes in bilayer structure upon protein incubation and the distribution of proteinaceous material along the bilayer normal are thus obtained. Using NR, we probed the structure of  $\zeta_{\text{cyt}}$  bound to stBLMs (POPC:POPG = 60:40 and POPC:POPS = 70:30) in buffers that contained 25 mM NaCl. Figure 5 shows an exemplary set of reflectivity curves for a POPC:POPS stBLM before and after addition of 15.8  $\mu\text{M}$   $\zeta_{\text{cyt}}$  in isotopically distinct buffers. Modelling established the corresponding nSLD distributions shown in the inset. Tables 1–3 contain median fit values and 68% confidence limits of the parameterized 1D structural profiles that give rise to these nSLD distributions for three distinct NR experiments.

In 25 mM NaCl, the distribution of  $\zeta_{\text{cyt}}$  as measured with protein in the buffer, occupies the hydrocarbon region and headgroups of the substrate-distal bilayer leaflet (Fig. 6A/C). Outside the bilayer, the peptide extends away from the membrane surface up to about 60 Å from the bilayer center. After rinsing with protein-free buffer, we observed significantly less bilayer-associated  $\zeta_{\text{cyt}}$  following bimodal distributions of proteinaceous material (Fig. 6B/D) with one peak within the hydrocarbon chains and the other  $\approx 40$ –50 Å from the membrane center.

In 150 mM NaCl, where electrostatic interactions are highly screened, the localization of membrane-bound  $\zeta_{\text{cyt}}$  depended on sample history. Protein incubation of the DOPC/DOPS bilayer that was previously exposed to  $\zeta_{\text{cyt}}$  in low-salt buffer and then rinsed (Fig. 6C/D), resulted in a distribution in which the protein on the membrane surface was essentially removed but membrane-embedded protein was unaffected (Fig. 7A). Subsequent rinsing with protein-free high-salt buffer removed some of the membrane-embedded  $\zeta_{\text{cyt}}$  (Fig. 7B). On the other hand, incubation of a pristine POPC/POPS bilayer with 15.8  $\mu\text{M}$   $\zeta_{\text{cyt}}$  resulted in a layer of protein peripherally associated with the membrane (Fig. 7C), and rinsing with protein-free buffer removed most of this protein (Fig. 7D).

The protein distributions measured at low salt concentrations (Fig. 6) can be interpreted as a single homogeneous protein configuration in which one region in the protein intercalates the membrane and another region extends substantially into the adjacent buffer phase. Alternatively, the same distributions would arise from two distinct protein populations of which one is membrane-inserted and a second one is peripherally associated with the membrane. The observation that rinsing with high-salt buffer removes the membrane-peripheral protein density but leaves the membrane-inserted density intact (Fig. 7A/B) suggests that latter model is correct. This conclusion is supported by Fig. 8 in which we quantitatively compare the protein distribution profiles on POPS-containing membranes at low and high ionic strength. The difference (red trace) between the profiles in 25 mM NaCl (black) and after subsequent incubation with protein in 150 mM NaCl (green) is identical to the protein distribution profile after incubation of a pristine membrane with  $\zeta_{\text{cyt}}$  at 150 mM NaCl (blue).

### *Accessibility of ITAMs in membrane-bound $\zeta_{\text{cyt}}$ to phosphorylation*

To investigate the effects of membrane interaction on phosphorylation of ITAM-tyrosine residues we used recombinant Lck-G2 $\Delta$  tyrosine kinase in a phosphorylation assay in which  $\zeta_{\text{cyt}}$  was exposed to large unilamellar POPC:POPG (60:40) vesicles (LUV). These experiments included 6.5 mM  $\text{Mg}^{2+}$  in the assay buffer, as previously described (19), to allow MgATP-dependent tyrosine kinase activity (37); the increase in ionic strength relative to 150 mM NaCl alone (12%) might weaken but is not likely to substantially alter the nature of the  $\zeta_{\text{cyt}}$ -membrane interaction. ( $\text{Ca}^{2+}$  at high local concentration has been reported to promote release from the membrane of ITAM-containing cytosolic domains (37), but  $\text{Mg}^{2+}$  interacts with acidic membrane more weakly than  $\text{Ca}^{2+}$  (38). As shown in Fig. 9, Lck phosphorylation of  $\zeta_{\text{cyt}}$  ITAM-tyrosines is reduced as the lipid concentration is increased. This decrease cannot be attributed to a lipid-dependent reduction of Lck catalytic activity, because a control experiment with an unrelated Fyn-substrate peptide does not depend on lipid concentration. In distinction from a previous study which showed that ITAMs on  $\zeta_{\text{cyt}}$  bound to lysomyristoylphosphatidylglycerol (LMPG) micelles were completely protected from phosphorylation (19), we observe only a partial reduction that levels off near 50% of the phos-

phorylation in the absence of lipid. Therefore, a fraction of tyrosine residues is still exposed to buffer or there is a dynamic equilibrium between the membrane-embedded and exposed populations. No significant differences in the time courses of  $\zeta_{\text{cyt}}$  phosphorylation were observed in the absence or presence of zwitterionic POPC LUVs (Fig. 10A), but substantial differences appeared in the presence of POPC/POPG LUVs, where phosphorylation kinetics slowed significantly at 0.5

## DISCUSSION

TCR  $\zeta_{\text{cyt}}$  (25) and CD3 $\epsilon_{\text{cyt}}$  (21) interact with the inner leaflet of the plasma membrane. Such interactions inhibit ITAM phosphorylation by Src-family kinases (19, 21) and may control the accessibility of ITAM tyrosines in the cellular context (19, 21, 39), providing regulatory mechanism for signal transmission. However, this hypothesis has been controversial, and mutations designed to disrupt membrane association can in some cases inhibit rather than potentiate tyrosine phosphorylation (25–27, 40, 41). This study was designed to shed light on this long-standing problem by investigating the membrane association of  $\zeta_{\text{cyt}}$  with well-defined membrane models and to correlate structural and functional aspects of protein-membrane association under well-controlled experimental conditions.

### *$\zeta_{\text{cyt}}$ adopts distinct conformations at the membrane*

The  $\zeta_{\text{cyt}}$ -membrane interaction has often been viewed as a simple equilibrium involving a single bound species (19, 20).  $\zeta_{\text{cyt}}$  is unstructured in solution but may adopt a helical structure in association with detergent micelles or acidic lipid vesicles, depending on detergent or lipid composition (19, 20, 22, 23). The SPR results in Fig. 3 confirm that  $\zeta_{\text{cyt}}$  membrane binding is contingent on acidic lipids. Not surprisingly, binding to charged membranes depends on ionic strength of the aqueous buffer because of electrostatic shielding by counterions (42). Accordingly, the dissociation constants,  $K_d \approx 4\text{--}6 \mu\text{M}$ , measured in 25 mM NaCl increase to  $> 25 \mu\text{M}$  in 150 mM NaCl, which is a lower limit because full binding isotherms could not be determined due to limited amounts of protein. This is consistent with a sucrose-loaded vesicle pull-down assay at 100 mM KCl that determined a molar partition coefficient  $K = 2,200 \text{ M}^{-1}$  for an equimolar mixture of POPC and POPG, and  $K = 84,000 \text{ M}^{-1}$  for 100 % POPG (20). Although the interaction of isolated  $\zeta_{\text{cyt}}$  is relatively weak, because the full-length  $\zeta$  domain is membrane anchored and the *local* concentration near

mM lipid compared to lipid-free phosphorylation, and only very slow phosphorylation was observed for 7 mM lipid (Fig. 10B). A similar delay in phosphorylation was observed in the presence of pure POPG LUVs, but equivalent levels of phosphorylation were reached at all LUV concentrations after long exposure times to the Lck kinase (Fig. 10C).

the membrane is therefore high, these results indicate a substantial and strong membrane interaction of the soluble domain by itself.

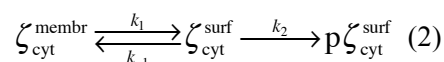
Examination of individual SPR traces in 25 mM NaCl after protein additions shows a slow decay that follows an initial spike (Fig. 3 B/C). Such a decay indicates a reduction of the refractive index of the interfacial layer which may result from a degradation of the lipid bilayer, i.e., formation of water-filled defects, or bilayer thinning, i.e., rearrangement of the aliphatic chains within the bilayer upon protein adsorption, or the replacement of lipid in the bilayer by protein which can outweigh the increase in refractive index due to peripherally-bound protein. EIS results show that bilayer integrity is maintained (Fig. 4), and therefore membrane degradation is unlikely to contribute to the observed changes in SPR. We observe that bilayer thinning is minimal upon protein incubation, with an upper limit of 5 % of the initial hydrocarbon thickness according to NR (Tables 1–3). This effect corresponds to an estimated reduction of 3–5 SPR response units at a protein concentration of  $\approx 16 \mu\text{M}$  where we observe SPR signals of  $> 30$  units (Fig. 3). Membrane thinning is therefore a component of the observed reduction in SPR response, but too small to account for much more than 10 % of the observed effects. The time courses of the SPR signals therefore most likely result from slow conformational changes of  $\zeta_{\text{cyt}}$  following its adsorption to the membrane surface. We propose a process in which  $\zeta_{\text{cyt}}$  initially binds peripherally to the membrane and converts to a second, membrane-embedded state thereafter, leading to a reduction in SPR response. NR corroborates this interpretation, as it shows proteinaceous material in two distinct distributions (Fig. 6 B/D) – one within the membrane and another that extends from the membrane surface into the buffer where it is selectively removed by rinsing (Fig. 7 A/B). We conclude that bound  $\zeta_{\text{cyt}}$  coexists in a membrane-embedded and in a membrane-peripheral state at low ionic strengths.

At physiological ionic strength (150 mM NaCl),  $\zeta_{\text{cyt}}$ 's interaction with the membrane is different: Individual SPR traces did not show bimodal time-courses (Fig. 3E) and membrane-bound protein does not penetrate the membrane, as shown by NR (Fig. 7C/D). We conclude that soluble  $\zeta_{\text{cyt}}$  interacts with the membrane too weakly or resides at the membrane too shortly to form a membrane-embedded state. However, this is only true for the truncated cytosolic domain of the protein, and hence the situation may differ for full-length  $\zeta$ , whose transmembrane segment ties the soluble protein region more tightly to the membrane.

While  $\zeta_{\text{cyt}}$  inserts deeply into the bilayer under conditions where it interacts strongly with the membrane, EIS shows that bilayer integrity is not compromised (Fig. 4). In addition to functional relevance of the membrane inserted state as a regulator of signal strength (see below), membrane insertion may also play a role in sensing or regulating local lipid curvature (43) or in intracellular sorting or trafficking (44, 45).

*$\zeta_{\text{cyt}}$  conformations are in a kinetic equilibrium*

Our studies of  $\zeta_{\text{cyt}}$  phosphorylation (Figs. 9, 10) correlate protein structure on the membrane with function and provide insight into the kinetics of the distinct protein conformations. We considered distinct kinetic models to interpret the data. First, we assumed that ITAM tyrosines of both peripherally bound and membrane-embedded  $\zeta_{\text{cyt}}$  populations were accessible to phosphorylation at different rate constants, such that the time course for  $p\zeta_{\text{cyt}}$  formation is a sum of two exponentials. Alternatively, only the peripherally bound  $\zeta_{\text{cyt}}$  population might be accessible to phosphorylation, such that  $p\zeta_{\text{cyt}}$  follows a single exponential with a rate constant similar to that in the absence of lipids. Here,  $p\zeta_{\text{cyt}}$  is limited by the number of exposed ITAM tyrosines, and due to inaccessibility of membrane-embedded protein, the final phosphorylation level will be lower than in the absence of lipids. Finally, we considered a dynamic equilibrium between membrane-embedded and peripherally bound  $\zeta_{\text{cyt}}$  where only the latter is accessible to phosphorylation. However, since phosphorylation of surface-bound  $\zeta_{\text{cyt}}$  reduces the interaction with acidic lipids (19, 20), this step is effectively irreversible:



If the sum of rate constants for interconversion of the surface-associated and membrane-inserted  $\zeta_{\text{cyt}}$  conformations ( $k_1+k_{-1}$ ) is similar to the phosphorylation rate ( $k_2$ ), a time lag in the formation of  $p\zeta_{\text{cyt}}$  is expected. While our experimental phosphorylation data are at odds with the first two models, the observed delay in  $\zeta_{\text{cyt}}$  phosphorylation in the presence of acidic vesicles (Fig. 10B, C) supports the latter, as it is reasonable to assume that the membrane-embedded conformation of  $\zeta_{\text{cyt}}$  is less susceptible to tyrosine phosphorylation. Therefore, it is likely that the two conformations are in a dynamic equilibrium, such that interaction of  $\zeta_{\text{cyt}}$  with the membrane does not fully abolish phosphorylation, but rather controls the reaction rate. The idea of a dynamic equilibrium between a membrane-associated and free state has also been suggested for the cytoplasmic domains of full length CD3 $\epsilon$  (41).

*A molecular model of the membrane-bound conformations of  $\zeta_{\text{cyt}}$*

Molecular models for membrane-associated  $\zeta_{\text{cyt}}$  consistent with the NR results took three considerations into account. First,  $\zeta_{\text{cyt}}$  is an unstructured protein in aqueous solution but interaction with lipid vesicles can induce helicity (19, 20, 23); in micellar solutions,  $\approx 35\%$  of the protein was  $\alpha$ -helical as observed by CD spectroscopy (22). Second, regions of  $\zeta_{\text{cyt}}$  that interact with acidic lipid headgroups have been mapped using single amino acid substitutions in the full-length  $\zeta$  (25), its cytoplasmic domain (27), and peptide fragments of  $\zeta_{\text{cyt}}$  (23, 27). These studies revealed basic-rich sequences (BRS, Fig. 11A) (25) at residues Lys40–Arg44, Lys51–Lys55 and Lys80–Lys87. Third, phosphorylation of ITAM tyrosines is blocked in LMPG micelles (19), suggesting sequestration of these residues into their hydrophobic cores. Accordingly, we designed molecular models with different levels of helicity in which tyrosine hydroxyls were sequestered by the membrane and most of the Lys and Arg side chains were in contact with phosphates or carboxylates of lipid headgroups. However, we were unable to generate membrane-embedded models consistent with the scattering profiles in which all Lys and Arg side chains of  $\zeta_{\text{cyt}}$  were outside the bilayer. Therefore, the final models contain four to seven buried Arg and four to six buried Lys residues. Because of the high energetic cost to immerse an arginine residue into a lipid bilayer, estimated at  $\sim 60$  kJ/mol (46), such models might seem unfavorable. However, TCR transmembrane domains

in close proximity within the intact receptor are replete with buried acid and basic residues, including Lys-Asp, Lys-Glu, and Arg-Asp salt bridges, with an excess of acidic residues (16). Moreover computer simulations suggest that transferring multiple Arg residues into lipid bilayers is energetically nonadditive (47), so that energetic penalty of burying multiple Arg sites might be lower than anticipated from single amino acid transfer studies and could be partially compensated by negative transfer energies for neighboring Leu, Ile and Val residues. We did not explicitly account for any potential temperature- or salt-dependent alterations in bilayer structure or protein stability, but these are not expected to be significant for the conditions investigated.

Potential helical peptide regions were assigned, as shown in Fig. 11, based upon hydropathy scores of the Kyte/Doolittle (48) and Wimley/White (49) hydrophobicity scales as well as secondary structure analysis (50) and guided the design of three models with different helical contents (Fig. 11C–E) with zero, 25% and 38% helicity. Scaled three-dimensional models of  $\zeta_{\text{cyt}}$  with these properties were placed into a mixed lipid bilayer with their N-terminal residues near the membrane surface and BRS residues preferentially in contact with lipid headgroups. Depending on whether the models were designed to conform to the NR-derived protein distribution profiles at 150 mM NaCl within or outside of the bilayer (Fig. 7A, B), ITAMs and their neighboring residues were either membrane-immersed or membrane-peripheral, as depicted in Figs. 12 or 13, respectively. For the membrane-embedded  $\zeta_{\text{cyt}}$  model, this implies that the central stretch of the peptide

## CONCLUSIONS

In this work, we presented an unconventional approach to quantify the role of protein-membrane interactions in regulating the accessibility of ITAM tyrosines, and thereby their phosphorylation, on the cytoplasmic  $\zeta$  domain of the T-cell receptor, a process that is at the root of signal transduction in T-cell signaling. While the impact of  $\zeta_{\text{cyt}}$  phosphorylation and its variation through membrane interactions have been extensively studied, mostly in the cellular context (25, 27), consensus on these processes has not been established due to contradicting results from distinct experiments (19, 26, 51, 52). In vitro experiments which reconstruct significant aspects of the T-cell receptor signaling cascade may help elucidate this

chain is located near the membrane surface while overall the protein may be anchored to the bilayer by its hydrophobic flanks (N-terminus to residue 30 and residue 90 to C-terminus), which may penetrate the bilayer deeply. Figures 12A–C show representative projections of the protein models with different helical contents. NR protein distribution profiles were calculated for these hypothetical models, scaled and compared with the experimental data. Fig. 12D shows that models of the membrane-embedded  $\zeta_{\text{cyt}}$  population agree well with the experimental data, independent of their helical content. The surface-associated  $\zeta_{\text{cyt}}$  configurations (Fig. 13), the protein is also ligated to the bilayer by its hydrophobic flanks but its hydrophilic central stretch forms loops that stretch out some 40 Å from the membrane surface, thus exposing the ITAM tyrosines to the aqueous compartment where they are easily accessible to phosphorylation by Src family kinases. Again, reconstructed nSLD profiles of proteins with distinct secondary structures, while indistinguishable, all capture the experimental result quite well. While these simple models are not unique, and thus not conclusive, they illustrate that peptide configurations which satisfy known constraints in conformational space can rationalize the NR results (Fig. 13D) and phosphorylation data. It will require more elaborate molecular dynamics simulations to quantify the underlying structures of the  $\zeta_{\text{cyt}}$  protein near membranes more stringently, explore the energetic landscapes that govern the distinct association modes and thus define the conditions that control interconversion between coexisting  $\zeta_{\text{cyt}}$  conformations.

problem (51, 52). Here we took the radical approach to study the soluble TCR  $\zeta_{\text{cyt}}$  domain in the extremely simple but well-controlled experimental environment of tethered synthetic bilayers probed by SPR and NR. This reductionist approach necessarily engenders certain compromises: we used soluble  $\zeta_{\text{cyt}}$  whereas in the native protein this domain is covalently attached to a transmembrane span, we modulated protein-lipid interaction by variation of solution ionic strength and lipid bilayer composition whereas in the physiological cellular environment the composition of aqueous and membrane phases are complex and dynamic, and we performed SPR and NR at subphysiological temperature because of instrumental constraints. Nonetheless, despite these caveats,

we were able to gain insight into basic features of the  $\zeta_{\text{cyt}}$ -membrane interaction.

The results presented here lead to a more complex concept of  $\zeta_{\text{cyt}}$ -membrane interactions than previously discussed. We determined the affinities of (soluble)  $\zeta_{\text{cyt}}$  to acidic membranes to be rather low, in the  $\mu\text{M}$  range, at low ionic strength and to drop further at physiological salt concentration. Despite this relatively weak interaction, in its native environment we expect that the  $\zeta_{\text{cyt}}$  component of the polytopic membrane-spanning TCR complex will be membrane-associated, as attested to by the observation of  $\zeta_{\text{cyt}}$ -membrane interaction in living cells (25, 28). The time courses of SPR adsorption traces indicated that the protein undergoes large-scale reconfiguration following adsorption to acidic membranes. The observation that the SPR signal *drops* slowly after a fast initial rise suggests – after exclusion of more trivial processes – that the protein inserts into the membrane. Indeed, corresponding phosphorylation assays with Lck showed that the ITAM accessibility of soluble

## MATERIALS AND METHODS

**Materials** – [ $\gamma$ - $^{32}\text{P}$ ]-ATP (3000 Ci/mmol) was from Perkin Elmer Life Science. Fyn kinase substrate (EFGTYGTLKSKK) was obtained from Enzo Life Science. 1-palmitoyl-2-oleoyl-*sn*-glycero-3-phosphocholine (POPC), 1-palmitoyl-2-oleoyl-*sn*-glycero-3-phospho-(1'-*rac*-glycerol) (POPG), and 1-palmitoyl-2-oleoyl-*sn*-glycero-3-phospho-L-serine (POPS) were from Avanti Polar Lipids.

### *Protein expression and purification*

The cytoplasmic domain (Lys51-Arg164) of human TCR $\zeta$  (NCBI Accession Number: NP\_000725.1) was cloned in pET32a(+) (Invitrogen) and expressed as a thrombin-cleavable Thioredoxin/His<sub>6</sub>-tagged protein in *E. coli* (strain BL21(DE3)) at 37 °C, as described (20), but with an additional purification step. Bacteria were harvested by centrifugation 4 h after induction with 1 mM IPTG and lysed under denaturing conditions using lysis buffer (10 mM TRIS, 100 mM NaH<sub>2</sub>PO<sub>4</sub>, pH 8, 8 M urea). Lysate was stirred for 12-16 hours at 4 °C and centrifuged at 10000 g. Supernatant was loaded onto Ni-NTA agarose (Qiagen) preequilibrated with lysis buffer. Protein was eluted by step-wise reduction of the pH (pH 6.3, 5.7, 4.5). Fractions containing  $\zeta_{\text{cyt}}$  were pooled and dialyzed against 20 mM HEPES pH 7.5, 150 mM NaCl, 1 mM DTT. Protein was digested with thrombin (MP Biomedicals, LLC) at 22 °C for 1 h

$\zeta_{\text{cyt}}$  is severely compromised in the presence of membranes. Two distinct membrane association states of  $\zeta_{\text{cyt}}$ , one deeply inserted and one peripherally bound, were also detected and characterized with NR, and it is tempting to assume that they are in a dynamic equilibrium at the membrane, as suggested by the phosphorylation assay. Both structures of the  $\zeta_{\text{cyt}}$ /membrane complexes clearly bear the signatures of molecular dimensions – one in which the central part of the protein that holds the ITAMs is membrane inserted and one in which it is solvent exposed. Even if we could not discriminate between distinct models with widely varying helicities, these results show clearly that the two association states must be grossly distinct in their functional roles: While the ITAM tyrosines are deeply buried within the membrane in the inserted state, they are exposed and thereby accessible to kinase activity in the membrane-peripheral state

in the presence of 5 mM CaCl<sub>2</sub> and 1 mM DTT. Digest was stopped by PMSF (0.5 mM), diluted with 50 mM MES pH 6 to a final NaCl concentration of 34 mM and loaded on cation exchange media (POROS HS20).  $\zeta_{\text{cyt}}$  elutes with a linear gradient of 120-360 mM NaCl. Fractions containing  $\zeta_{\text{cyt}}$  were identified by SDS-PAGE (12.5 % TRIS/Tricine gels) and further purified by RP-HPLC on a C18 Vydac 22 × 250 mm preparative column with a linear gradient of 5-80 % acetonitrile containing 0.05 % TFA (v/v). Fractions containing  $\zeta_{\text{cyt}}$  were lyophilized, dissolved in 150 mM NH<sub>4</sub>HCO<sub>3</sub>, pH 8.5 and purified by size-exclusion chromatography on a Superdex 200 10/300 (GE Healthcare Life Science) column. After final lyophilization,  $\zeta_{\text{cyt}}$  was stored at -20 °C.

Recombinant Lck-G2 $\Delta$  (N-terminal glycine deleted to prevent myristoylation) containing SH3, SH2, and catalytic kinase domains was expressed using High Five™ cells infected with recombinant Baculovirus (a gift from M. Eck) at a multiplicity of infection of 0.1 pfu/cell. Cells were harvested by centrifugation 72 hours after infection, resuspended in 25 mM HEPES pH 7.4, 25 mM NaCl, 2 mM DTT, 0.5 mM PMSF and leupeptin, aprotinin, pepstatin (2  $\mu\text{g}/\text{ml}$  each) and lysed by sonication. Lysate was centrifuged (75000 g, 1 hour) and the supernatant loaded on a 5 mL HiLoad DEAE FF-column (GE Healthcare) preequilibrated with 25 mM HEPES, pH 7.4, 25 mM NaCl. Protein elutes with linear gradient of

25-500 mM NaCl. Fractions containing Lck were pooled and applied to gel filtration chromatography (Superdex 200 16/60) in 25 mM HEPES, pH 7.7, 150 mM NaCl. Further purification was performed after concentrating Lck-containing fractions (Amicon Ultra 4 30 k filter unit) and buffer-exchange (25 mM TRIS, pH 8.5) by anion-exchange chromatography (POROS HQ20). Protein elutes with a linear gradient of 300-400 mM NaCl. Pooled fractions were stored at -80 °C.

#### *Vesicle preparation*

Definite amounts of lipids dissolved in chloroform were well mixed to obtain homogeneity of chosen lipid compositions. Chloroform was evaporated under a continuous N<sub>2</sub>-stream and completely removed by lyophilization. Lipids were hydrated in 20 mM HEPES, pH 7.4, 150 mM NaCl and subjected to five freeze-thaw cycles. Large unilamellar vesicles (LUVs) were prepared by extrusion (11 times) through a stack of two polycarbonate filters (pore size of 100 nm) using an Avanti Mini-Extruder (Avanti Polar Lipids). Vesicles were characterized by negative-stain electron microscopy and dynamic light scattering. Dynamic light scattering experiments were performed with a DynaPro-MS800 (Protein Solutions) instrument at 20 °C. Samples of LUVs (2 mM) were incubated at 20 °C with or without ζ<sub>cyt</sub> (45 μM) in 20 mM HEPES, pH 7.5, 25 mM NaCl, diluted (1:10000) and filtered (Millex filter unit 0.22 μM) prior to measurements. Scattering data were analyzed using DYNAMICS autocorrelation analysis software (version 5.25.44).

Samples analyzed by negative-stain electron microscopy were prepared by incubating LUVs (3 mM) with or without ζ<sub>cyt</sub> (10 μM) in 20 mM HEPES, pH 7.7, 150 mM NaCl, 6.5 mM MgCl<sub>2</sub> and applied to carbon-coated Formvar 300-mesh gold grids, stained with 1 % (w/v) uranyl acetate solution. Micrographs were taken with a Philips CM10 transmission electron microscope equipped with a Gatan CCD camera system.

#### *Preparation of sparsely tethered lipid bilayer membranes*

Sparsely tethered phospholipid bilayer membranes (stBLMs) were prepared on gold-coated silicon wafers (NR) or 1×3" microscopy glass slides (SPR) by vesicle fusion as previously described (34). Briefly, freshly gold-coated substrates using magnetron sputtering (ATC Orion, AJA) were immersed overnight in a 0.2 mM solution of a tether lipid, Z-20-(Z-octadec-9-enyloxy)-3,6,9,12,15,18,22-hepta-oxa-tetracont-31-ene-1-

thiol (HC18) as described (34), and β-mercaptoethanol (βME; Sigma-Aldrich) mixed at molar ratio 3:7 in ethanol to form mixed self-assembled monolayers (SAMs). The substrates were then rinsed with pure ethanol and dried in a N<sub>2</sub>-stream and stBLMs formed by incubating the SAM with a 10 mg/mL phospholipid vesicle solution in 1 M NaCl, 20 mM HEPES, pH 7.4 for 1h. The sample was finally rinsed with copious amounts of 0.25 M NaCl, 20 mM HEPES, pH 7.4.

#### *Surface plasmon resonance*

SPR measurements were conducted at 25 (±0.01) °C in a single-batch set-up using a custom-built instrument (SPR Biosystems, Germantown). SAM-covered, gold-coated glass slides were assembled in the Kretschmann configuration by index-matching to a prism. stBLMs were completed by vesicle fusion in situ, as described above. The setup allows for simultaneous SPR and electrochemical impedance spectroscopy (EIS) measurements, which is used to assess the quality of the stBLMs before and after protein is introduced. In the single-batch experiments, the neat bilayer is measured first to determine a baseline before adding protein in increasing concentrations  $c_p$  and measuring the equilibrium SPR response  $R_{eq}$ .  $R_{eq}(c_p)$  was fitted to the Langmuir isotherm to determine the protein affinity in terms of the dissociation constant  $K_d$ , and the surface density,  $R_\infty$ , of bound protein extrapolated to infinite concentration  $c_p$ :

$$R_{eq}(c_p) = \frac{c_p R_\infty}{c_p + K_d}$$

#### *Electrochemical Impedance Spectroscopy*

EIS data were taken using a Solartron (Farnborough, U.K.) system (model 1287A potentiostat and model 1260 frequency response analyzer). Au-coated glass slides served as the working electrode in a setup that allowed simultaneous SPR and EIS measurements. The cell has a volume  $V \approx 250 - 300 \mu\text{L}$  and a surface area  $A_{el} \approx 0.33 \text{ cm}^2$  confined by a Viton O-ring. Copper contrast was used to measure the geometric electrode surface area (53) and raw EIS data were normalized to  $A_{el}$  and a roughness factor  $\beta = 1.4$ , estimated from the Au surface oxidation/oxide stripping charge (54). A saturated silver-silver chloride (Ag|AgCl|NaCl(aq,sat)) microelectrode (Microelectrodes, model M-401F) was used as reference. The auxiliary electrode was a 0.25 mm diameter platinum wire (99.99% purity, Sigma-Aldrich) coiled around the barrel of the reference electrode.

The distance between the tip of the reference and working Au electrode surface was set to 2 – 3 mm. Measurements were carried out in aerated solutions with 10 mV a.c. at 0 V bias vs. reference electrode. Data analysis was carried out by fitting to an equivalent circuit using ZView (Scribner Associates), as described (33).

#### *Neutron reflectometry*

NR measurements were performed at  $22 \pm 2$  °C on the NGD-MAGIK reflectometer at the NIST Center for Neutron Research (NCNR) (55). Reflectivity curves were recorded for momentum transfer values  $0.008 \text{ \AA}^{-1} \leq q_z \leq 0.25 \text{ \AA}^{-1}$ . stBLMs were prepared on 3" diameter Si wafers assembled in a flow cell (56). Samples were measured at room temperature using three isotopically different bulk solvents of distinct H/D contrasts ( $D_2O$ ,  $H_2O$ , and a 2:1 (v/v) mixture of the two), with adequate counting statistics typically obtained after  $\approx 6$  h. The flow cell allows for in situ buffer exchange; therefore, subsequent measurements were performed on the same sample area. NR data were first collected from an as-prepared stBLM. Thereafter, protein was added to the stBLM and NR data were collected either during protein incubation or after rinsing the bilayer with buffer.

To characterize the structures of proteins associated with the membrane, one-dimensional (1D) neutron scattering length density (nSLD) profiles along the lipid bilayer normal were determined by fitting to the experimental NR data. These 1D structural profiles were composed using a hybrid of a stratified slab model for the solid substrate (57), a continuous distribution of lipid components for the stBLM (58) and a monotonic Hermite spline for the model-free envelope of the protein (36). In this compound model, bulk silicon, silicon oxide, a chromium bonding layer ( $\approx 50 \text{ \AA}$ ), and the substrate-terminal gold layer ( $\approx 150 \text{ \AA}$ ) were parameterized as subsequent slabs in terms of thickness and nSLD for each layer, except for the bulk Si for which the nSLD is known. One global roughness parameter was applied to all substrate interfaces. Individual sub-molecular groups implemented in the continuous distribution model of the stBLM are:  $\beta$ ME, tether PEG chains, tether glycerol groups, substrate-proximal and substrate-distal PC and PS headgroups, substrate-proximal and substrate-distal methylene and methyl chains of lipid and tether molecules. Fit parameters are the bilayer hydrocarbon thickness for each bilayer leaflet, bilayer completeness, tether surface density, tether thickness,  $\beta$ ME surface density, and one

roughness parameter applied to all these distributions.

The Hermite spline that encodes the protein distribution profile is defined by control points that are on average  $20 \text{ \AA}$  apart. The number of control points depends on the spatial extension of the protein along the bilayer normal and is determined iteratively during model optimization. Fit parameters for each control point are the volume occupancy of protein and the deviation from a position defined by equidistant control points throughout the spline. A constant nSLD is associated with the spline functions that thus describe the contributions to the scattering of either completely protiated or partially deuterated, intrinsically homogeneous protein material.

Data modeling was performed with the *ga\_refl* and *Refl1D* software packages (56) using a differential evolution Markov chain global optimizer. Reflectivity curves recorded from one sample under different conditions were fitted simultaneously to the same model by sharing fit parameters, for example, for the solid substrate. The recorded Monte Carlo Markov Chain was used to determine the fit parameter confidence limits using a statistical analysis. This procedure yields a bias-free and objective estimate of the uncertainties of the resulting nSLD profiles while avoiding over-parameterization (36).

#### *Molecular modeling*

Two amino acid residues (Gly1, Ser2) were N-terminally appended to the primary sequence of  $\zeta_{\text{cyt}}$  to account for the thrombin recognition site in the recombinant protein. Residue numbering used here refers to the cytosolic domain of  $\zeta$ , such that residue Leu 51 in the native full length protein (with signal sequence) is considered number 3. The hydrophathy score and the secondary structure prediction were determined using ExPASy ProtScale (59) and PSIPRED v3.3 (50), respectively. Molecular models were derived from an initial ideal helix model, which was interspersed with perturbations to maintain helical segments at the desired positions. Three-dimensional conformations of these initial models were adjusted using Lego tools in the O software environment (60) to reflect local conformations found in a library of high resolution protein structures. Final protein models were used to form a protein/membrane system by using the CHARMM-GUI Input Generator (61). Protein structures were first pre-oriented relative to the membrane normal, then surrounded by lipid-like

spheres whose positions were subsequently replaced by lipid molecules (replacement method). A rectangular protein/membrane system was formed choosing DOPC/DOPS molecules in a molar ratio of 70:30.

*Tyrosine phosphorylation assay*

Phosphorylation of  $\zeta_{\text{cyt}}$  (2  $\mu\text{M}$ ), or Fyn kinase substrate (150  $\mu\text{M}$ ) by recombinant Lck (0.2  $\mu\text{M}$ ) was performed in 20 mM HEPES, pH 7.4, 150 mM NaCl, 6.5 mM  $\text{MgCl}_2$ , 50  $\mu\text{M}$   $\text{Na}_3\text{VO}_4$ ,

112.5  $\mu\text{M}$  ATP (0.25  $\mu\text{Ci}/\mu\text{L}$  [ $\gamma^{32}\text{P}$ ]-ATP) at 37 °C with or without vesicles. Reaction was stopped by adding 20  $\mu\text{L}$  of 40 % trichloroacetic acid to 40  $\mu\text{L}$  of phosphorylation mixture. Aliquots of 30  $\mu\text{L}$  were transferred to P81 phosphocellulose squares (Millipore), washed extensively with 0.75 % phosphoric acid and air dried. Incorporation of  $^{32}\text{P}$  was quantified by scintillation counting (Wallac MicroBeta<sup>2</sup> 1450, Perkin Elmer).

**Acknowledgements:** We thank Michael J. Eck (Harvard Medical School) for recombinant baculovirus and appreciate the help from Lara Strittmatter and Gregory M. Hendricks (University of Massachusetts Medical School, Electron Microscopy Facility, Project S10RR027897). This work was supported by the NIH through grants AI-38996 (LJS) and GM-101647 (ML) and by the Department of Commerce through its Measurement Science and Engineering program (70NANB13H009) and the IMS program “Precision Measurement for Integral Membrane Proteins”. Parts of this research were performed at the NIST Center for Nanoscale Science. Certain commercial materials, equipment, and instruments are identified in this work to describe the experimental procedure as completely as possible. In no case does such an identification imply a recommendation or endorsement by National Institute of Standards and Technology, nor does it imply that the materials, equipment, or instrument identified are necessarily the best available for the purpose.

**Conflict of interest:** The authors declare that they have no conflicts of interest with the contents of this article.

**Author contributions:** K. Z., R. E., F. H., S. R., B. J. and P. S. conducted experiments and analyzed results. K. Z. generated three-dimensional protein models. K. Z., F. H., M. L. and L. J. S. wrote the paper. M. L. and L. J. S. conceived the idea.

## REFERENCES

1. Rudolph, M. G., Stanfield, R. L., and Wilson, I. A. (2006) How TCRs bind MHCs, peptides, and coreceptors. *Annu. Rev. Immunol.* **24**, 419–466
2. Reth, M. (1989) Antigen receptor tail clue. *Nature.* **338**, 383–384
3. Irving, B. A., and Weiss, A. (1991) The cytoplasmic domain of the T cell receptor  $\zeta$  chain is sufficient to couple to receptor-associated signal transduction pathways. *Cell.* **64**, 891–901
4. Frigault, M. J., and Maus, M. V. (2016) Chimeric antigen receptor-modified T cells strike back. *Int. Immunol.* **28**, 355–363
5. Garcia, K. C., Degano, M., Stanfield, R. L., Brunmark, A., Jackson, M. R., Peterson, P. A., Teyton, L., and Wilson, I. A. (1996) An  $\alpha\beta$  T cell receptor structure at 2.5 Å and its orientation in the TCR-MHC complex. *Science.* **274**, 209–219
6. Yin, Y., Li, Y., Kerzic, M. C., Martin, R., and Mariuzza, R. A. (2011) Structure of a TCR with high affinity for self-antigen reveals basis for escape from negative selection. *EMBO J.* **30**, 1137–1148
7. Sun, Z.-Y. J., Kim, S. T., Kim, I. C., Fahmy, A., Reinherz, E. L., and Wagner, G. (2004) Solution structure of the CD3 $\epsilon\delta$  ectodomain and comparison with CD3 $\epsilon\gamma$  as a basis for modeling T cell receptor topology and signaling. *Proc. Natl. Acad. Sci. U. S. A.* **101**, 16867–16872
8. Kjer-Nielsen, L., Dunstone, M. A., Kostenko, L., Ely, L. K., Beddoe, T., Mifsud, N. A., Purcell, A. W., Brooks, A. G., McCluskey, J., and Rossjohn, J. (2004) Crystal structure of the human T cell receptor CD3 $\epsilon\gamma$  heterodimer complexed to the therapeutic mAb OKT3. *Proc. Natl. Acad. Sci. U. S. A.* **101**, 7675–7680
9. Arnett, K. L., Harrison, S. C., and Wiley, D. C. (2004) Crystal structure of a human CD3- $\epsilon/\delta$  dimer in complex with a UCHT1 single-chain antibody fragment. *Proc. Natl. Acad. Sci. U. S. A.* **101**, 16268–16273
10. Birnbaum, M. E., Berry, R., Hsiao, Y.-S., Chen, Z., Shingu-Vazquez, M. A., Yu, X., Waghray, D., Fischer, S., McCluskey, J., Rossjohn, J., Walz, T., and Garcia, K. C. (2014) Molecular architecture of the  $\alpha\beta$  T cell receptor–CD3 complex. *Proc. Natl. Acad. Sci.* **111**, 17576–17581
11. He, Y., Rangarajan, S., Kerzic, M., Luo, M., Chen, Y., Wang, Q., Yin, Y., Workman, C. J., Vignali, K. M., Vignali, D. A. A., Mariuzza, R. A., and Orban, J. (2015) Identification of the docking site for CD3 on the T cell receptor  $\beta$  chain by solution NMR. *J. Biol. Chem.* **290**, 19796–19805
12. Natarajan, A., Nadarajah, V., Felsovalyi, K., Wang, W., Jeyachandran, V. R., Wasson, R. A., Cardozo, T., Bracken, C., and Krogsgaard, M. (2016) Structural model of the extracellular assembly of the TCR-CD3 complex. *Cell Rep.* **14**, 2833–2845
13. Call, M. E., Schnell, J. R., Xu, C., Lutz, R. A., Chou, J. J., and Wucherpfennig, K. W. (2006) The structure of the  $\zeta\zeta$  transmembrane dimer reveals features essential for its assembly with the T cell receptor. *Cell.* **127**, 355–368
14. Petruk, A. A., Varriale, S., Coscia, M. R., Mazzarella, L., Merlino, A., and Oreste, U. (2013) The structure of the CD3  $\zeta\zeta$  transmembrane dimer in POPC and raft-like lipid bilayer: A molecular dynamics study. *Biochim. Biophys. Acta - Biomembr.* **1828**, 2637–2645
15. Sharma, S., Lensink, M. F., and Juffer, A. H. (2014) The structure of the CD3 $\zeta\zeta$  transmembrane dimer in lipid bilayers. *Biochim. Biophys. Acta - Biomembr.* **1838**, 739–746
16. Call, M. E., Pyrdol, J., Wiedmann, M., and Wucherpfennig, K. W. (2002) The organizing principle in the formation of the T cell receptor-CD3 complex. *Cell.* **111**, 967–979
17. Lee, M. S., Glassman, C. R., Deshpande, N. R., Badgandi, H. B., Parrish, H. L., Uttamapinant, C., Stawski, P. S., Ting, A. Y., and Kuhns, M. S. (2015) A mechanical switch couples T cell receptor triggering to the cytoplasmic juxtamembrane regions of CD3 $\zeta\zeta$ . *Immunity.* **43**, 227–239
18. Weissenhorn, W., Eck, M. J., Harrison, S. C., and Wiley, D. C. (1996) Phosphorylated T cell receptor  $\zeta$ -chain and ZAP70 tandem SH2 domains form a 1:3 Complex in Vitro. *Eur. J.*

- Biochem.* **238**, 440–445
19. Aivazian, D., and Stern, L. J. (2000) Phosphorylation of T cell receptor  $\zeta$  is regulated by a lipid dependent folding transition. *Nat. Struct. Biol.* **7**, 1023–1026
  20. Sigalov, A. B., Aivazian, D., Uversky, V. N., and Stern, L. J. (2006) Lipid-binding activity of intrinsically unstructured cytoplasmic domains of multichain immune recognition receptor signaling subunits. *Biochemistry.* **45**, 15731–15739
  21. Xu, C., Gagnon, E., Call, M. E., Schnell, J. R., Schwieters, C. D., Carman, C. V., Chou, J. J., and Wucherpfennig, K. W. (2008) Regulation of T cell receptor activation by dynamic membrane binding of the CD3 $\epsilon$  cytoplasmic tyrosine-based motif. *Cell.* **135**, 702–713
  22. Duchardt, E., Sigalov, A. B., Aivazian, D., Stern, L. J., and Schwalbe, H. (2007) Structure induction of the T-cell receptor  $\zeta$ -chain upon lipid binding investigated by NMR spectroscopy. *Chembiochem.* **8**, 820–827
  23. Sigalov, A. B., and Hendricks, G. M. (2009) Membrane binding mode of intrinsically disordered cytoplasmic domains of T cell receptor signaling subunits depends on lipid composition. *Biochem. Biophys. Res. Commun.* **389**, 388–393
  24. Laczkó, I., Hollósi, M., Vass, E., Hegedűs, Z., Monostori, É., and Tóth, G. K. (1998) Conformational effect of phosphorylation on T-cell receptor/CD3 $\zeta$ -chain sequences. *Biochem. Biophys. Res. Commun.* **242**, 474–479
  25. Zhang, H., Cordoba, S.-P., Dushek, O., and van der Merwe, P. A. (2011) Basic residues in the T-cell receptor  $\zeta$  cytoplasmic domain mediate membrane association and modulate signaling. *Proc. Natl. Acad. Sci.* **108**, 19323–19328
  26. DeFord-Watts, L. M., Tassin, T. C., Becker, A. M., Medeiros, J. J., Albanesi, J. P., Love, P. E., Wülfing, C., and van Oers, N. S. C. (2009) The cytoplasmic tail of the T cell receptor CD3 $\epsilon$  subunit contains a phospholipid-binding motif that regulates T cell functions. *J. Immunol.* **183**, 1055–1064
  27. DeFord-Watts, L. M., Dougall, D. S., Belkaya, S., Johnson, B. a, Eitson, J. L., Roybal, K. T., Barylko, B., Albanesi, J. P., Wülfing, C., and van Oers, N. S. C. (2011) The CD3  $\zeta$  subunit contains a phosphoinositide-binding motif that is required for the stable accumulation of TCR-CD3 complex at the immunological synapse. *J. Immunol.* **186**, 6839–6847
  28. Shi, X., Bi, Y., Yang, W., Guo, X., Jiang, Y., Wan, C., Li, L., Bai, Y., Guo, J., Wang, Y., Chen, X., Wu, B., Sun, H., Liu, W., Wang, J., and Xu, C. (2013) Ca<sup>2+</sup> regulates T-cell receptor activation by modulating the charge property of lipids. *Nature.* **493**, 111–115
  29. Romeo, C., and Seed, B. (1991) Cellular immunity to HIV activated by CD4 fused to T cell or Fc receptor polypeptides. *Cell.* **64**, 1037–1046
  30. Letourneur, F., and Klausner, R. D. (1991) T-cell and basophil activation through the cytoplasmic tail of T-cell-receptor  $\zeta$  family proteins. *Proc. Natl. Acad. Sci. U. S. A.* **88**, 8905–8909
  31. Romeo, C., Amiot, M., and Seed, B. (1992) Sequence requirements for induction of cytolysis by the T cell antigen/Fc receptor  $\zeta$  chain. *Cell.* **68**, 889–897
  32. Bridgeman, J. S., Ladell, K., Sheard, V. E., Miners, K., Hawkins, R. E., Price, D. A., and Gilham, D. E. (2014) CD3 $\zeta\zeta$ -based chimeric antigen receptors mediate T cell activation via cis- and trans-signalling mechanisms: Implications for optimization of receptor structure for adoptive cell therapy. *Clin. Exp. Immunol.* **175**, 258–267
  33. McGillivray, D. J., Valincius, G., Vanderah, D. J., Febo-Ayala, W., Woodward, J. T., Heinrich, F., Kasianowicz, J. J., and Lösche, M. (2007) Molecular-scale structural and functional characterization of sparsely tethered bilayer lipid membranes. *Biointerphases.* **2**, 21–33
  34. Budvytyte, R., Valincius, G., Niaura, G., Voiciuk, V., Mickevicius, M., Chapman, H., Goh, H. Z., Shekhar, P., Heinrich, F., Shenoy, S., Lösche, M., and Vanderah, D. J. (2013) Structure and properties of tethered bilayer lipid membranes with unsaturated anchor molecules. *Langmuir.* **29**, 8645–8656

35. McGillivray, D. J., Valincius, G., Heinrich, F., Robertson, J. W. F., Vanderah, D. J., Febo-Ayala, W., Ignatjev, I., Lösche, M., and Kasianowicz, J. J. (2009) Structure of functional *Staphylococcus aureus*  $\alpha$ -hemolysin channels in tethered bilayer lipid membranes. *Biophys. J.* **96**, 1547–1553
36. Heinrich, F., and Lösche, M. (2014) Zooming in on disordered systems: Neutron reflection studies of proteins associated with fluid membranes. *Biochim. Biophys. Acta - Biomembr.* **1838**, 2341–2349
37. Sun, G., and Budde, R. J. A. (1997) Requirement for an additional divalent metal cation to activate protein tyrosine kinases. *Biochemistry.* **36**, 2139–2146
38. McLaughlin, A., Grathwohl, C., and McLaughlin, S. (1978) The Adsorption of Divalent Cations to Phosphatidylcholine Bilayer Membranes. *Biochim. Biophys. Acta.* **513**, 338–357
39. Kuhns, M. S., and Davis, M. M. (2008) The Safety on the TCR Trigger. *Cell.* **135**, 594–596
40. Fernandes, R. A., Yu, C., Carmo, A. M., Evans, E. J., van der Merwe, A. P., and Davis, S. J. (2010) What controls T cell receptor phosphorylation? *Cell.* **142**, 668–669
41. Gagnon, E., Xu, C., Yang, W., Chu, H. H., Call, M. E., Chou, J. J., and Wucherpfennig, K. W. (2010) Multilayered control of T cell receptor phosphorylation. *Cell.* **142**, 669–671
42. Ben-Tal, N., Honig, B., Miller, C., and McLaughlin, S. (1997) Electrostatic binding of proteins to membranes. Theoretical predictions and experimental results with charybdotoxin and phospholipid vesicles. *Biophys. J.* **73**, 1717–1727
43. Drin, G., and Antonny, B. (2010) Amphipathic helices and membrane curvature. *FEBS Lett.* **584**, 1840–1847
44. Liu, H., Rhodes, M., Wiest, D. L., and Vignali, D. A. A. (2000) On the dynamics of TCR:CD3 complex cell surface expression and downmodulation. *Immunity.* **13**, 665–675
45. Szymczak, A. L., and Vignali, D. A. A. (2005) Plasticity and rigidity in adaptor protein-2-mediated internalization of the TCR:CD3 complex. *J Immunol.* **174**, 4153–4160
46. MacCallum, J. L., Bennett, W. F. D., and Tieleman, D. P. (2007) Partitioning of amino acid side chains into lipid bilayers: results from computer simulations and comparison to experiment. *J. Gen. Physiol.* **129**, 371–377
47. MacCallum, J. L., Bennett, W. F. D., and Tieleman, D. P. (2011) Transfer of arginine into lipid bilayers is nonadditive. *Biophys. J.* **101**, 110–117
48. Kyte, J., and Doolittle, R. F. (1982) A simple method for displaying the hydropathic character of a protein. *J. Mol. Biol.* **157**, 105–132
49. Wimley, W. C., and White, S. H. (1996) Experimentally determined hydrophobicity scale for proteins at membrane interfaces. *Nat. Struct. Biol.* **3**, 284–289
50. McGuffin, L. J., Bryson, K., and Jones, D. T. (2000) The PSIPRED protein structure prediction server. *Bioinformatics.* **16**, 404–5
51. Hui, E., and Vale, R. D. (2014) In vitro membrane reconstitution of the T-cell receptor proximal signaling network. *Nat. Struct. Mol. Biol.* **21**, 133–142
52. Furlan, G., Minowa, T., Hanagata, N., and Kataoka-Hamai, C. (2014) Phosphatase CD45 both positively and negatively regulates T cell receptor phosphorylation in reconstituted membrane protein clusters. *J. Biol. Chem.* **289**, 28514–28525
53. Vanderah, D. J., Gates, R. S., Silin, V., Zeiger, D. N., Woodward, J. T., Meuse, C. W., Valincius, G., and Nickel, B. (2003) Isostructural self-assembled monolayers. 1. Octadecyl 1-thiaoligo(ethylene oxides). *Langmuir.* **19**, 2612–2620
54. Trasatti, S., and Petrii, O. A. (1991) Real surface area measurements in electrochemistry. *Pure Appl. Chem.* **63**, 711–734
55. Dura, J. A., Pierce, D. J., Majkrzak, C. F., Maliszewskyj, N. C., McGillivray, D. J., Lösche, M., O'Donovan, K. V., Mihailescu, M., Perez-Salas, U., Worcester, D. L., and White, S. H. (2006) AND/R: Advanced neutron diffractometer/reflectometer for investigation of thin films and

- multilayers for the life sciences. *Rev. Sci. Instrum.* **77**, 1–11
56. Kirby, B. J., Kienzle, P. A., Maranville, B. B., Berk, N. F., Krycka, J., Heinrich, F., and Majkrzak, C. F. (2012) Phase-sensitive specular neutron reflectometry for imaging the nanometer scale composition depth profile of thin-film materials. *Curr. Opin. Colloid Interface Sci.* **17**, 44–53
  57. Ankner, J., and Majkrzak, C. (1992) Subsurface profile refinement for neutron specular reflectivity (Invited Paper). *Proceedings SPIE 1738, Neutron Opt. Devices Appl.*
  58. Shekhar, P., Nanda, H., Lösche, M., and Heinrich, F. (2011) Continuous distribution model for the investigation of complex molecular architectures near interfaces with scattering techniques. *J. Appl. Phys.* **110**, 102216
  59. Gasteiger Elisabeth, Hoogland Christine, Gattiker Alexander, Duvaud S'everine, Wilkins Marc R., Appel Ron D., and Bairoch, A. (2005) *Protein Identification and Analysis Tools on the ExPASy Server* (Walker, J. M. ed), Humana Press, Totowa, NJ
  60. Jones, T. A., Zou, J. Y., and Cowan, S. W. (1991) Improved methods for building protein models in electron density maps and the location of errors in these models. *Acta Crystallogr. Sect. A Found. Crystallogr.* **47**, 110–119
  61. Jo, S., Kim, T., Iyer, V. G., and Im, W. (2008) CHARMM-GUI: a web-based graphical user interface for CHARMM. *J. Comput. Chem.* **29**, 1859–1865

## FIGURE LEGENDS

**FIGURE 1:** The T cell antigen receptor is formed by eight single-pass transmembrane proteins. Subunits TCR $\alpha$  and  $\beta$  which interact with extracellular MHC-peptide complexes, form a disulfide-bonded heterodimer. The heterodimers CD3 $\gamma\epsilon$  and CD3 $\delta\epsilon$  associate with TCR $\alpha\beta$  through their extracellular and transmembrane domains. A disulfide-bonded homodimer of  $\zeta$ -subunits interacts through its transmembrane domains with TCR $\alpha\beta$ . CD3 $\gamma$ ,  $\delta$ ,  $\epsilon$  and TCR $\zeta$  form substantial cytosolic domains that contain immunoreceptor tyrosine-based activation motifs (open circles).

**FIGURE 2:** Molecular-scale illustration of the stBLMs used in studies of  $\zeta_{\text{cyt}}$  incubation by SPR and NR. Synthetic lipids tethered to a 10 nm thick gold film contain an oligo(ethylene oxide) segment that separates a lipid bilayer from the atomically flat gold surface which is passivated by co-adsorption of  $\beta$ ME. The hydrated space between the  $\beta$ ME film and the bilayer avoids direct contacts between the membrane and the solid surface. This configuration is sufficiently resilient to withstand buffer exchanges by flowing solutions across the bilayer.

**FIGURE 3:** SPR responses to  $\zeta_{\text{cyt}}$  incubations of stBLMs composed of (A) POPC, (B) POPC/POPG = 60:40, (C) POPC/POPS = 70:30, (D) DOPC/DOPS/cholesterol = 65:35:3, all in 25 mM NaCl, and (E) POPC/POPS = 70:30 in 150 mM NaCl. Left panels: Solution concentrations of  $\zeta_{\text{cyt}}$ , indicated in the plots, elicit spikes in SPR response at the time of injection which are due to temporary perturbations of the interface while adding the protein. Panels on the right show the responses as a function of  $\zeta_{\text{cyt}}$  concentration and fits to the Langmuir adsorption model where applicable.

**FIGURE 4:** Cole-Cole plots and ECM fits to EIS data of a POPC/POPS = 70:30 stBLM before and after SPR  $\zeta_{\text{cyt}}$  binding measurements at concentrations between 0.05  $\mu\text{M}$  and 23  $\mu\text{M}$  in 25 mM NaCl over 4 h (see Fig. 4C). The bilayer capacity increased insignificantly from 0.93(2)  $\mu\text{F cm}^{-2}$  to 0.96(2)  $\mu\text{F cm}^{-2}$ , while its resistance decreased from 255(21)  $\text{k}\Omega \text{ cm}^2$  exposure to 139(26)  $\text{k}\Omega \text{ cm}^2$  during the SPR measurements. This indicates minor protein-induced defect formation in the bilayer but rules out large-scale bilayer reorganization. Similar results were obtained for other combined SPR/EIS experiments (not shown).

**FIGURE 5:** NR data and best fits for an stBLM (POPC/POPS = 70:30) without protein and with 15.8  $\mu\text{M}$   $\zeta_{\text{cyt}}$  in two isotopically distinct bulk solvents ( $\text{H}_2\text{O}$  and  $\text{D}_2\text{O}$ -based buffer, 25 mM NaCl). The inset shows the nSLD profiles from which fits to the reflectivity were computed. These profiles are an intermediate step in the modeling process and represent the scattering properties of the material along the surface. They derive from a primary model that in turn represents the molecular architecture of the interfacial film in terms of the stBLM and protein, which is chemistry-based and referred to as composition-space model (see Figs. 6-8).

**FIGURE 6:** Composition-space modeling results of NR data for stBLMs exposed to 15.8  $\mu\text{M}$   $\zeta_{\text{cyt}}$  in buffers containing 25 mM NaCl. (A, B): Component volume occupancy (CVO) profiles of a POPC/POPG = 60:40 stBLM during protein exposure (A) and after rinse with protein-free buffer (B). (C, D): CVO profiles of a POPC/POPS = 70:30 stBLM during protein exposure (C) and after rinse with protein-free buffer (D).

**FIGURE 7:** Composition-space modeling results of NR data for stBLMs exposed to 15.8  $\mu\text{M}$   $\zeta_{\text{cyt}}$  in buffers containing 150 mM NaCl. (A, B): CVO profiles during protein exposure (A) and after rinse with protein-free buffer (B) showing the same POPC/POPS=70:30 stBLM that was initially exposed to  $\zeta_{\text{cyt}}$  at 25 mM NaCl (Fig. 6). (B, C): CVO profiles from a pristine POPC/POPS = 70:30 stBLM during protein exposure (C) and after rinse with protein-free buffer (D).

**FIGURE 8:** Comparison of protein distribution (CVO) profiles from NR experiments on POPC/POPS = 70:30 stBLMs exposed to 15.8  $\mu\text{M}$   $\zeta_{\text{cyt}}$  in buffers containing 25 mM and 150 mM NaCl. Subsequent incubations with  $\zeta_{\text{cyt}}$  in 25 mM NaCl (black trace, Fig. 6C) and 150 mM NaCl (green trace, Fig. 7A) lead to the removal of the membrane-peripheral fraction of protein (red trace, difference plot) while the membrane-embedded fraction remains. An independent protein incubation of a pristine stBLM at 150 mM NaCl yields a membrane-peripheral CVO profile (blue trace, Fig. 7C) that is quantitatively consistent with the difference plot (red trace).

**FIGURE 9:** Phosphorylation of  $\zeta_{\text{cyt}}$  (2  $\mu\text{M}$ , squares) and Fyn-substrate peptide (500  $\mu\text{M}$ , triangles) as control by Lck as a function of lipid concentration (LUVs, POPC/POPG = 60:40). Circles indicate Lck without substrate.

**FIGURE 10:** Phosphorylation of  $\zeta_{\text{cyt}}$  (2  $\mu\text{M}$ ) in the absence of lipids (open squares) and, shown with filled symbols, in the presence of LUVs composed of (A) POPC, (B) POPC/POPG = 60:40 and (C) POPG. Error bars represent SD. P-values < 0.05 (from Student's t-test) are represented by \*.

**FIGURE 11:** (A) Primary sequence of  $\zeta_{\text{cyt}}$  with two extra N-terminal amino acid residues (Gly, Ser) resulting from the thrombin recognition site. Arginine and lysine residues are highlighted in blue, key residues of ITAMs (tyrosine, leucine/isoleucine) are shown in magenta. (B) Hydropathy scores of the Kyte/Doolittle (48) (black line) and Wimley/White (49) (blue line) hydrophobicity scales and secondary structure prediction based on amino acid sequence. Locations of predicted  $\alpha$  helices with 0 % (C), 25 % (D) and 38 % (E) overall helical content used to construct molecular models.

**FIGURE 12:**  $\zeta_{\text{cyt}}$  models with distinct helical contents (A: zero, B: 25 %, C: 38 %) embedded in a lipid bilayer.  $\alpha$ -helical segments are shown in red, key ITAM residues (Tyr, Leu/Ile) in magenta and Arg/Lys sidechains in blue. (D) NR protein distribution profiles calculated for these models are compared with the experimental data (black) in 25 mM NaCl.

**FIGURE 13:**  $\zeta_{\text{cyt}}$  models with distinct helical contents (A: zero, B: 25 %, C: 38 %) peripherally bound to a lipid bilayer. Sections in the  $\zeta_{\text{cyt}}$ -sequences arranged into  $\alpha$ -helices are highlighted in red. Color code as in Fig. 12.

## Tables

**Table 1:** Median fit parameters and 68 % confidence limits for the NR experiment using a 70:30 POPC:POPG stBLM and 15.8  $\mu\text{M}$   $\zeta_{\text{cyt}}$  at 25 mM NaCl.

Parameter	Neat bilayer	15.8 $\mu\text{M}$ $\zeta_{\text{cyt}}$ , 25 mM NaCl	Rinse, 25 mM NaCl
<b>Substrate</b>			
Thickness $\text{SiO}_x$ layer / $\text{\AA}$		$16.1 \pm 2.4$	
nSLD $\text{SiO}_x$ layer / $10^{-6} \text{\AA}^{-2}$		$3.44 \pm 0.08$	
thickness Cr layer / $\text{\AA}$		$26.1 \pm 2.8$	
nSLD Cr layer / $10^{-6} \text{\AA}^{-2}$		$2.96 \pm 0.07$	
Thickness Au layer / $\text{\AA}$		$173.0 \pm 0.9$	
nSLD Au layer / $10^{-6} \text{\AA}^{-2}$		$4.50 \pm 0.01$	
<b>Bilayer</b>			
Thickness tether / $\text{\AA}$		$10.9 \pm 0.2$	
Molar fraction of tether in the inner lipid leaflet		$0.65 \pm 0.17$	
Number of $\beta\text{Me}$ molecules per tether molecule		$2.2 \pm 0.7$	
Hydrocarbon thickness, inner lipid leaflet / $\text{\AA}$	$17.1 \pm 0.4$	Change: $-1.5 \pm 0.9$	Change: $+1.3 \pm 0.1$
Hydrocarbon thickness, outer lipid leaflet / $\text{\AA}$	$12.0 \pm 1.1$		
Bilayer completeness	$1.00 \pm 0.01$	$1.00 \pm 0.01$	$1.00 \pm 0.01$
<b>Peptide</b>			
Amount of membrane-associated protein, protein volume / $\text{\AA}^3$	n/a	$8.6 \pm 1.6$	$3.6 \pm 0.3$
Fraction of protein in hydrocarbon region	n/a	$0.12 \pm 0.04$	$0.25 \pm 0.06$
Fraction of protein in head-group region	n/a	$0.16 \pm 0.03$	$0.05 \pm 0.03$
Fraction of protein in bulk solvent region	n/a	$0.71 \pm 0.05$	$0.70 \pm 0.04$

**Table 2:** Median fit parameters and 68 % confidence limits for the NR experiment using a 70:30 POPC:POPS stBLM and a subsequent incubation of 15.8  $\mu\text{M}$   $\zeta_{\text{cyt}}$  at 25 mM and 150 mM NaCl.

Parameter	Neat bi-layer	15.8 $\mu\text{M}$ $\zeta_{\text{cyt}}$ , 25 mM NaCl	Rinse, 25 mM NaCl	15.8 $\mu\text{M}$ $\zeta_{\text{cyt}}$ , 150 mM NaCl	Rinse, 150 mM NaCl
<b>Substrate</b>					
Thickness $\text{SiO}_x$ layer / $\text{\AA}$	16.2 $\pm$ 2.6				
nSLD $\text{SiO}_x$ layer / $10^{-6} \text{\AA}^{-2}$	3.52 $\pm$ 0.09				
thickness Cr layer / $\text{\AA}$	34.5 $\pm$ 2.6				
nSLD Cr layer / $10^{-6} \text{\AA}^{-2}$	3.04 $\pm$ 0.02				
Thickness Au layer / $\text{\AA}$	161.0 $\pm$ 0.5				
nSLD Au layer / $10^{-6} \text{\AA}^{-2}$	4.48 $\pm$ 0.01				
<b>Bilayer</b>					
Thickness tether / $\text{\AA}$	10.8 $\pm$ 0.4				
Molar fraction of tether in the inner lipid leaflet	0.59 $\pm$ 0.22				
Number of $\beta\text{Me}$ molecules per tether molecule	1.7 $\pm$ 0.8				
Hydrocarbon thickness, inner lipid leaflet / $\text{\AA}$	19.3 $\pm$ 1.4	Change: -1.2 $\pm$ 0.7	Change: +0.1 $\pm$ 0.3	Change: -0.2 $\pm$ 0.8	Change: +0.2 $\pm$ 0.3
Hydrocarbon thickness, outer lipid leaflet / $\text{\AA}$	12.7 $\pm$ 1.3				
Bilayer completeness	0.99 $\pm$ 0.01	0.99 $\pm$ 0.01	1.00 $\pm$ 0.01	0.99 $\pm$ 0.01	0.88 $\pm$ 0.02
<b>Peptide</b>					
Amount of membrane-associated protein, protein volume / $\text{\AA}^3$	n/a	9.1 $\pm$ 2.0	1.6 $\pm$ 0.7	3.7 $\pm$ 1.3	2.5 $\pm$ 0.7
Fraction of protein in hydrocarbon region	n/a	0.20 $\pm$ 0.07	0.40 $\pm$ 0.09	0.59 $\pm$ 0.14	0.54 $\pm$ 0.12
Fraction of protein in head-group region	n/a	0.15 $\pm$ 0.04	0.14 $\pm$ 0.05	0.19 $\pm$ 0.07	0.11 $\pm$ 0.05
Fraction of protein in bulk solvent region	n/a	0.64 $\pm$ 0.08	0.46 $\pm$ 0.07	0.20 $\pm$ 0.09	0.35 $\pm$ 0.12

**Table 3:** Median fit parameters and 68 % confidence limits for the NR experiment using a 70:30 POPC:POPS stBLM and 15.8  $\mu\text{M}$   $\zeta_{\text{cyt}}$  at 150 mM NaCl.

Parameter	Neat bilayer	15.8 $\mu\text{M}$ $\zeta_{\text{cyt}}$ , 25 mM NaCl	Rinse, 25 mM NaCl
<b>Substrate</b>			
Thickness $\text{SiO}_x$ layer / $\text{\AA}$	17.6 $\pm$ 2.7		
nSLD $\text{SiO}_x$ layer / $10^{-6} \text{\AA}^{-2}$	3.61 $\pm$ 0.08		
thickness Cr layer / $\text{\AA}$	28.8 $\pm$ 2.7		
nSLD Cr layer / $10^{-6} \text{\AA}^{-2}$	3.12 $\pm$ 0.06		
Thickness Au layer / $\text{\AA}$	154.2 $\pm$ 0.6		
nSLD Au layer / $10^{-6} \text{\AA}^{-2}$	4.53 $\pm$ 0.01		
<b>Bilayer</b>			
Thickness tether / $\text{\AA}$	12.2 $\pm$ 0.2		
Molar fraction of tether in the inner lipid leaflet	0.47 $\pm$ 0.21		
Number of $\beta\text{Me}$ molecules per tether molecule	1.7 $\pm$ 0.8		
Hydrocarbon thickness, inner lipid leaflet / $\text{\AA}$	19.5 $\pm$ 0.6	Change: -0.2 $\pm$ 0.3	Change: -0.4 $\pm$ 0.3
Hydrocarbon thickness, outer lipid leaflet / $\text{\AA}$	13.7 $\pm$ 0.7		
Bilayer completeness	1.00 $\pm$ 0.01	1.00 $\pm$ 0.01	1.00 $\pm$ 0.01
<b>Peptide</b>			
Amount of membrane-associated protein, protein volume / $\text{\AA}^3$	n/a	3.0 $\pm$ 0.6	2.0 $\pm$ 0.3
Fraction of protein in hydrocarbon region	n/a	0.09 $\pm$ 0.04	0.12 $\pm$ 0.06
Fraction of protein in head-group region	n/a	0.08 $\pm$ 0.03	0.05 $\pm$ 0.04
Fraction of protein in bulk solvent region	n/a	0.82 $\pm$ 0.07	0.73 $\pm$ 0.09

Figure 1

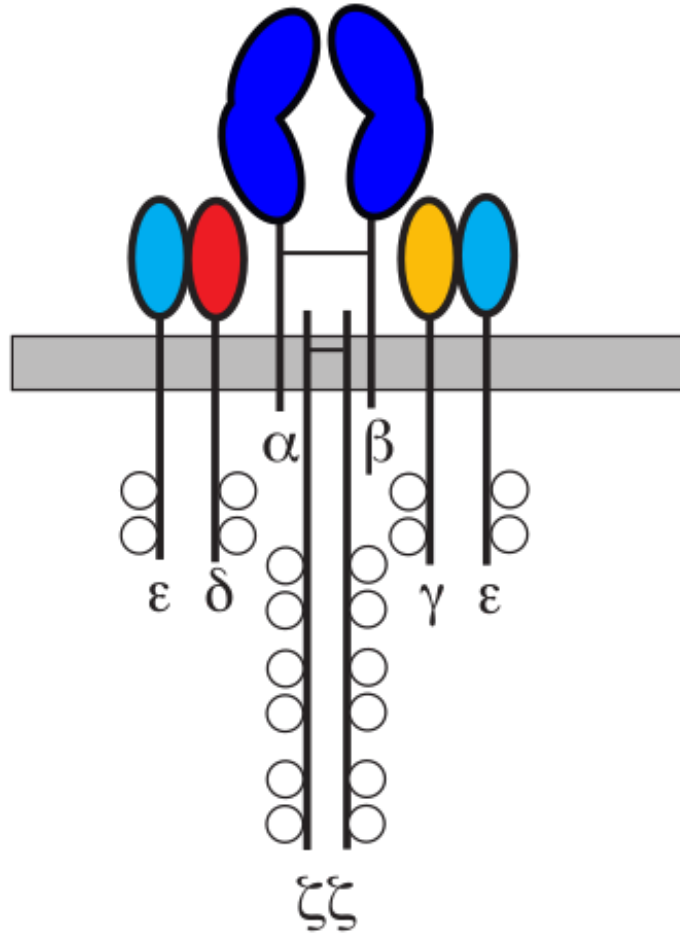
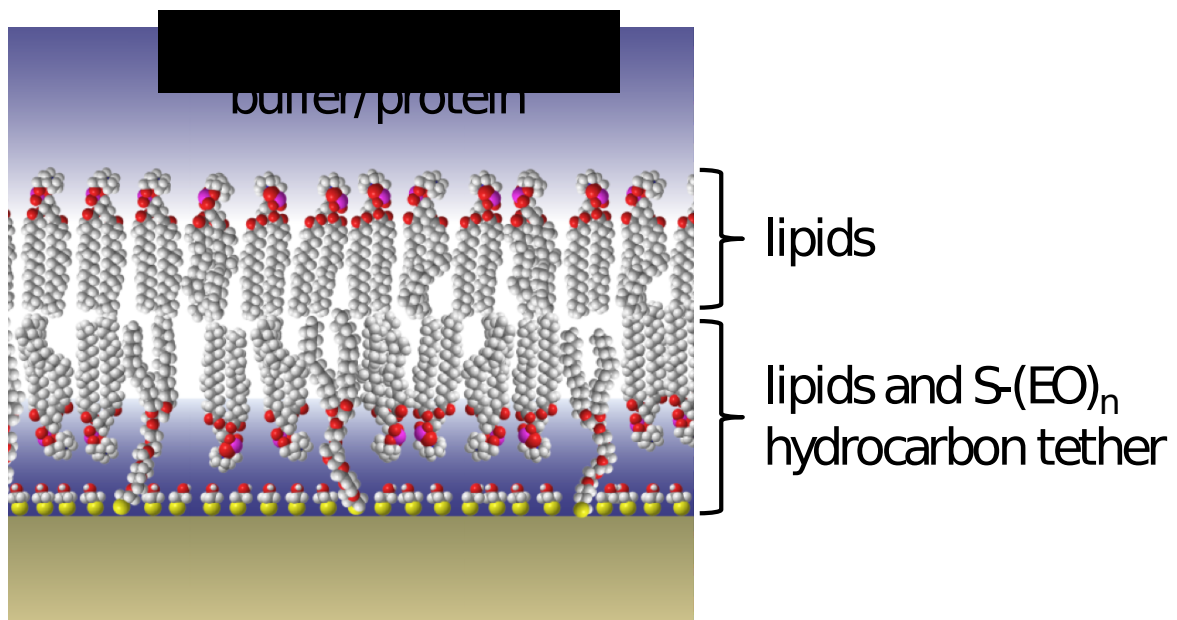


Figure 2



# Figure 3

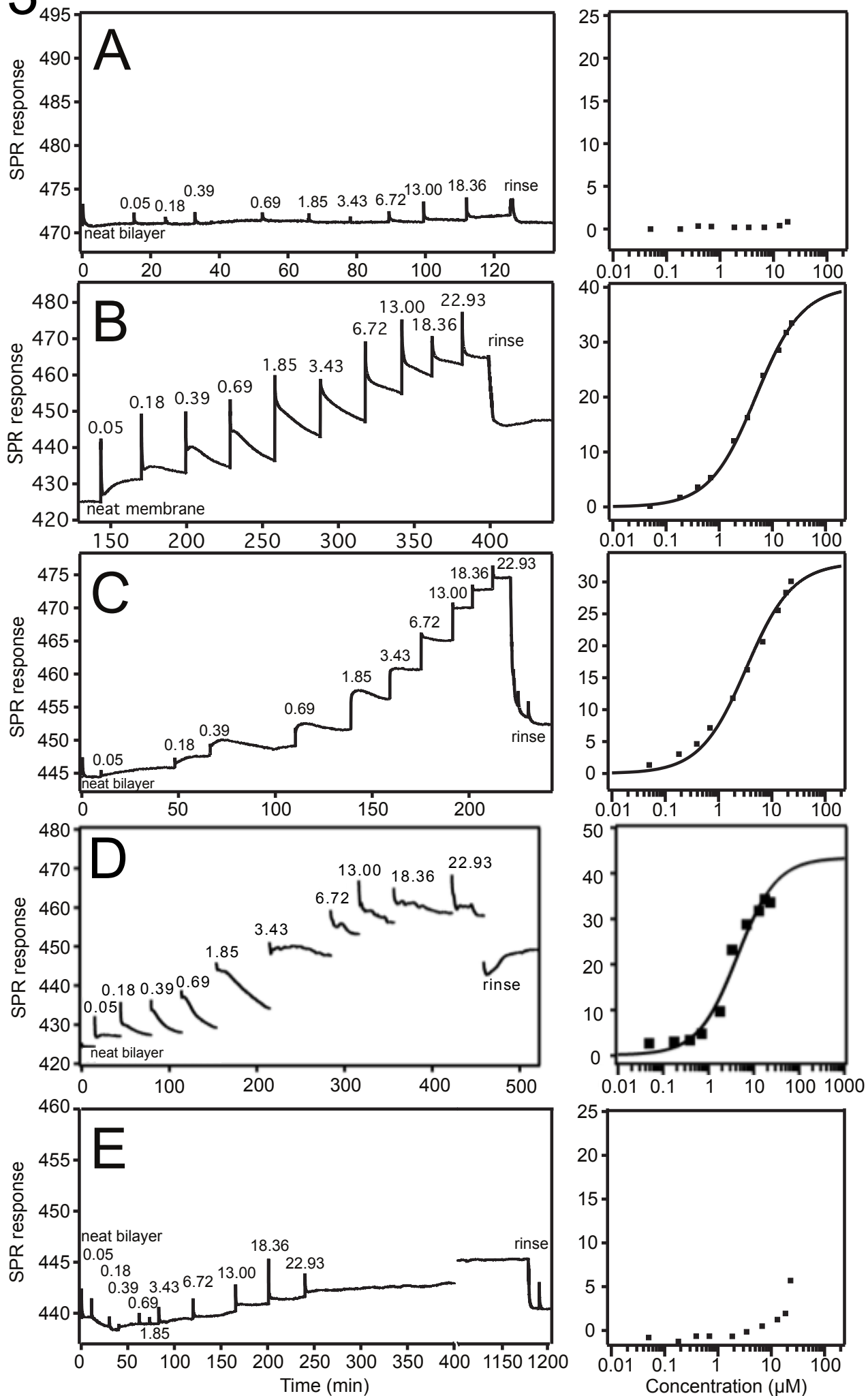


Figure 4

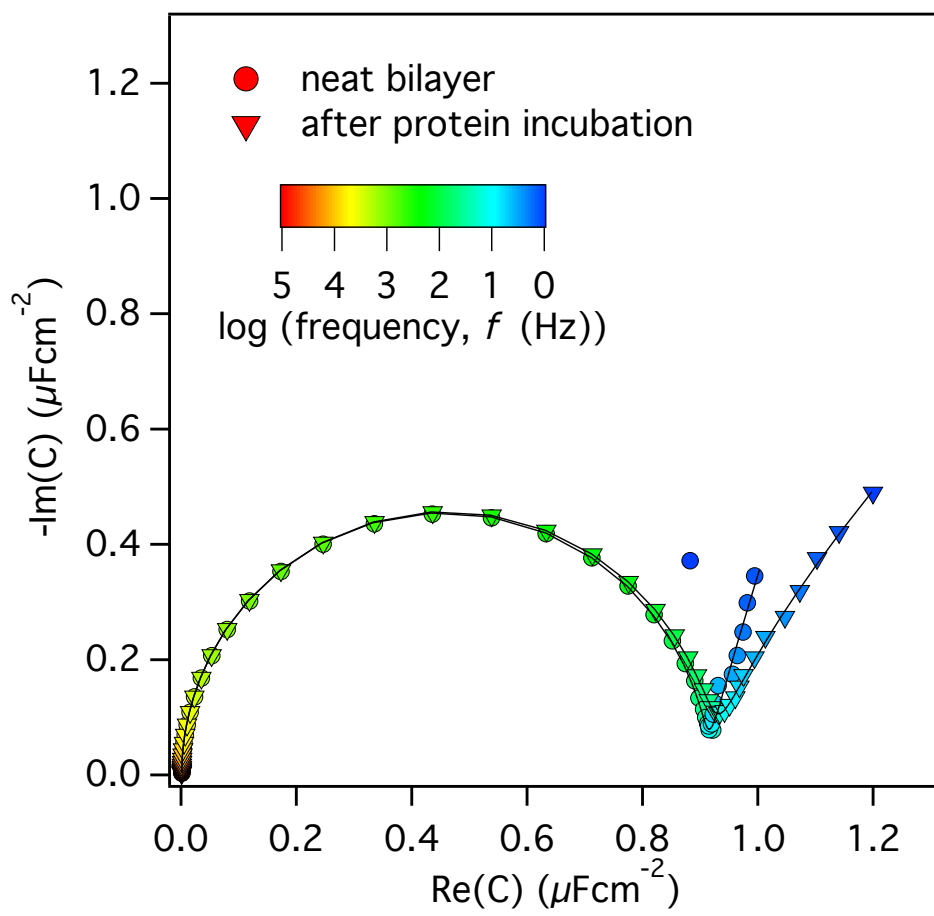


Figure 5

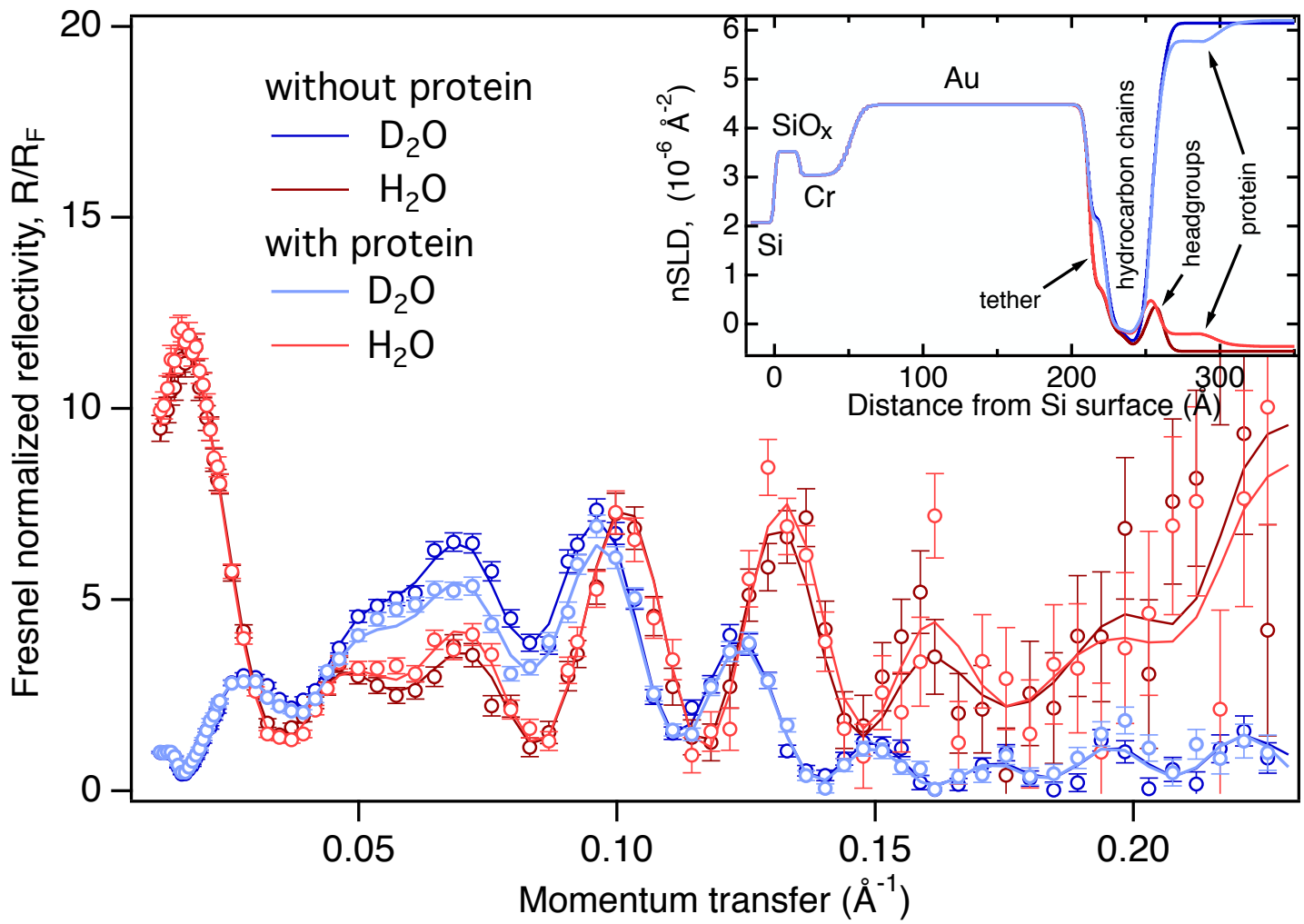


Figure 6

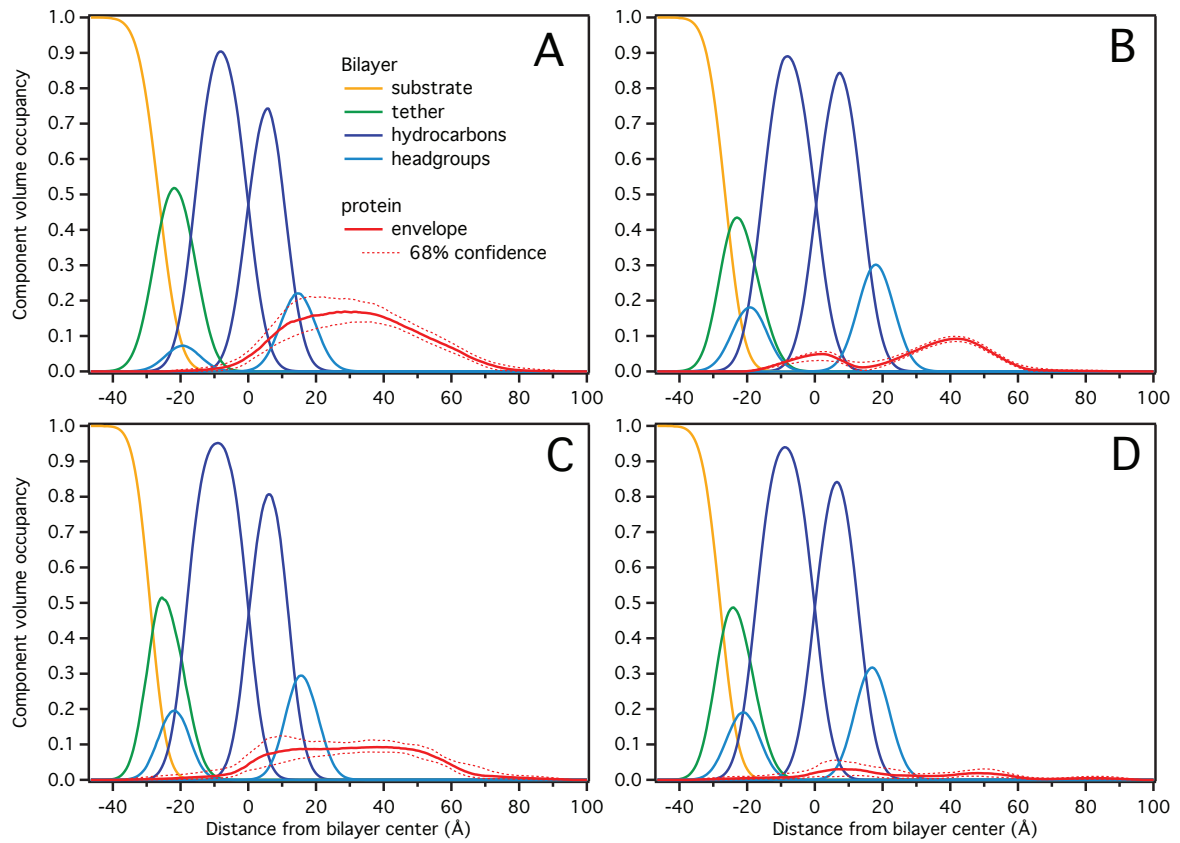


Figure 7

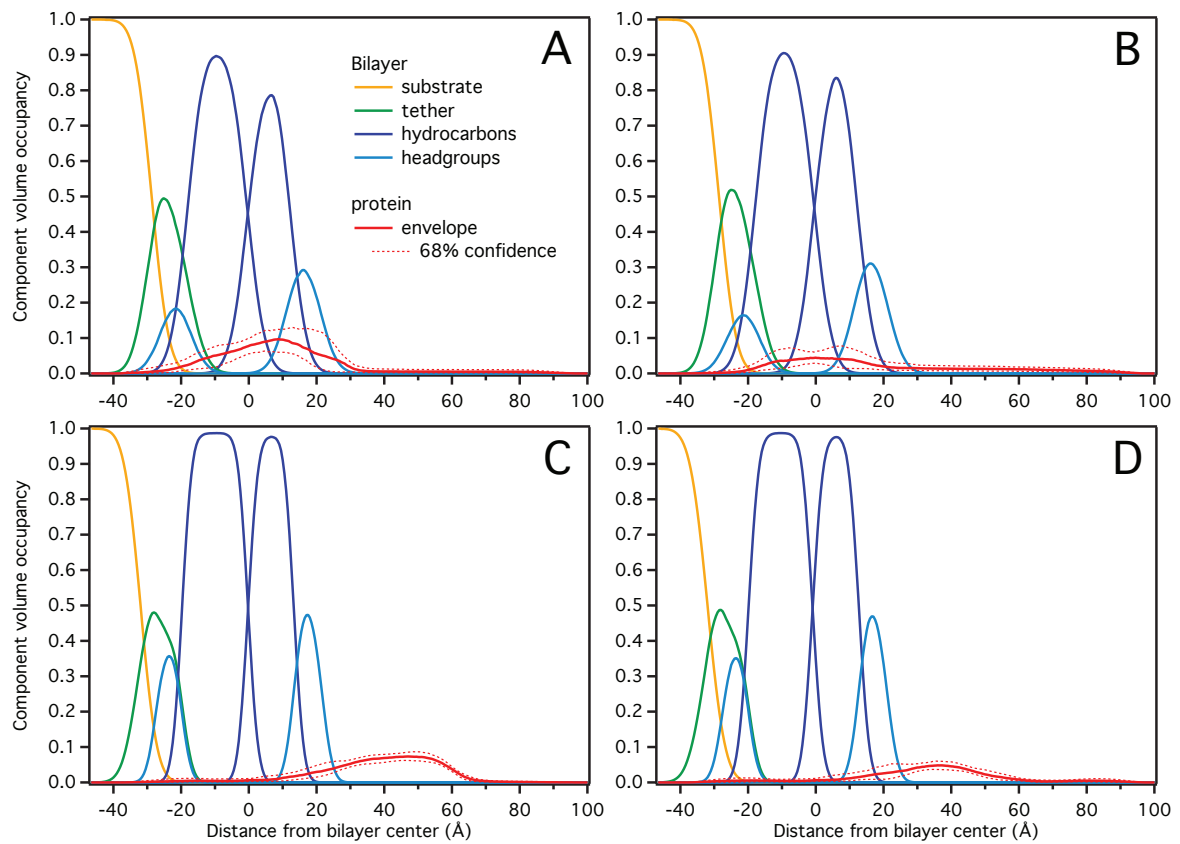


Figure 8

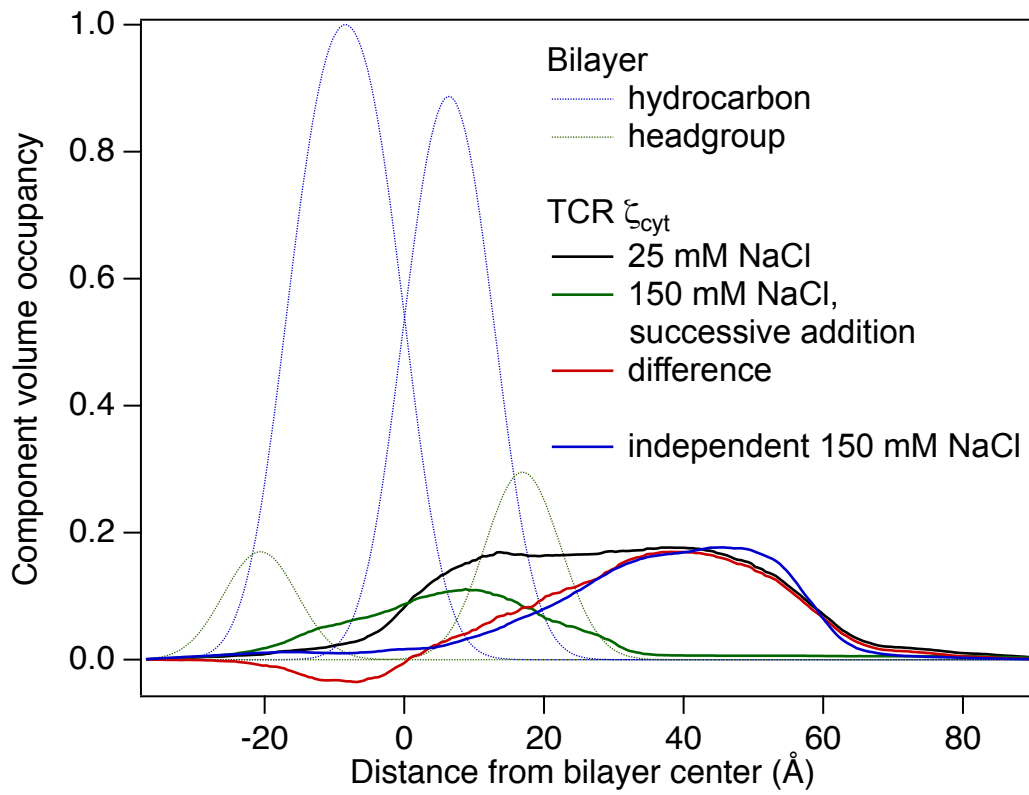


Figure 9

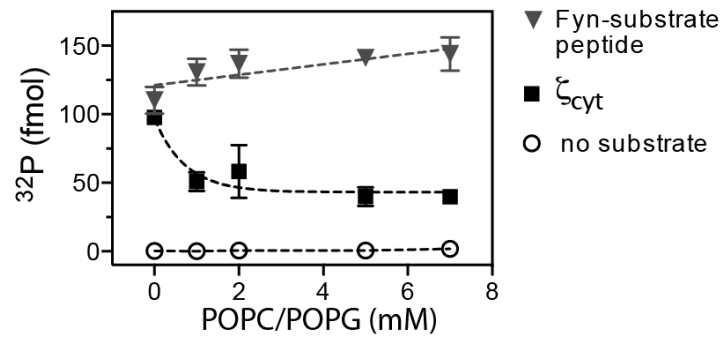


Figure 10

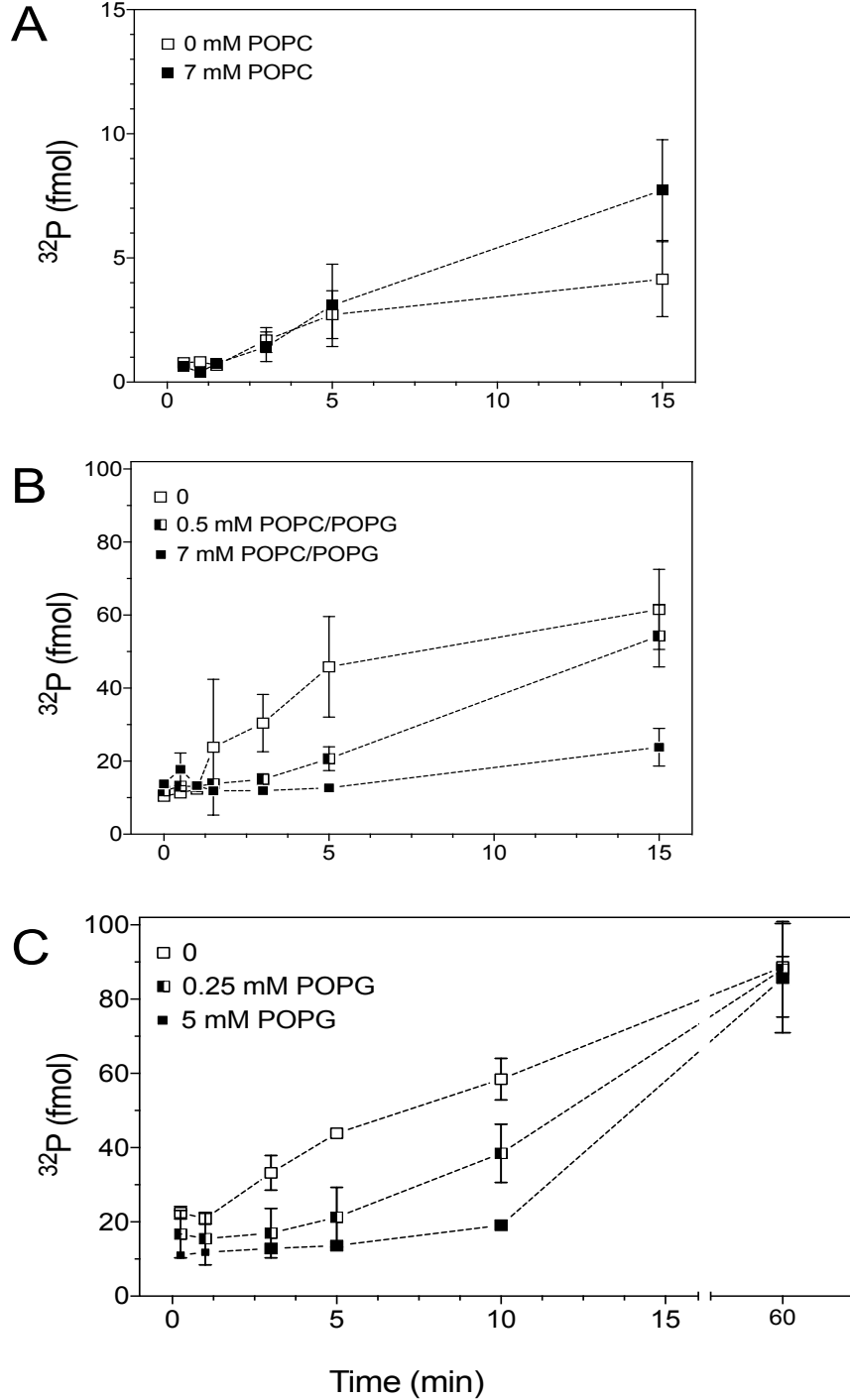


Figure 11

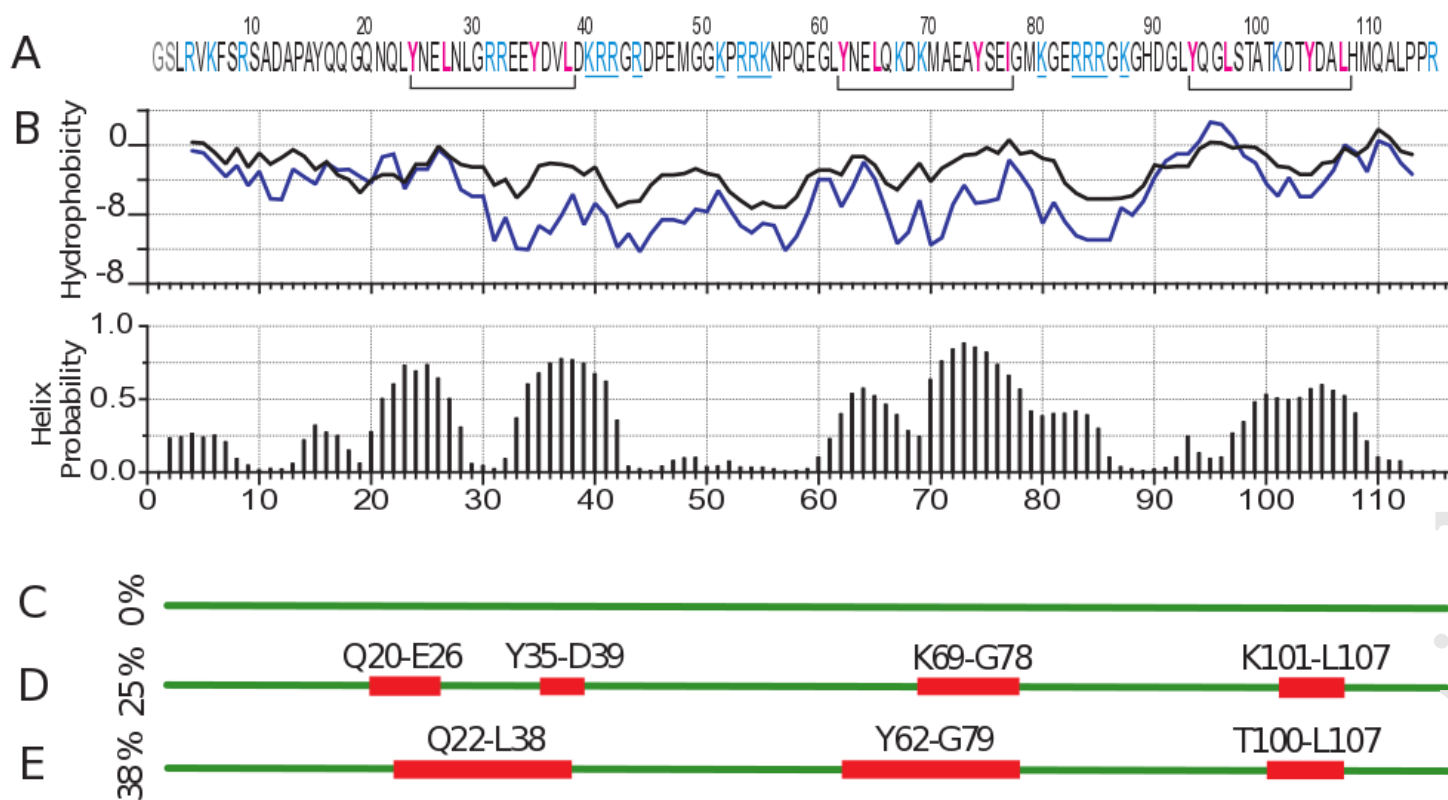


Figure 12

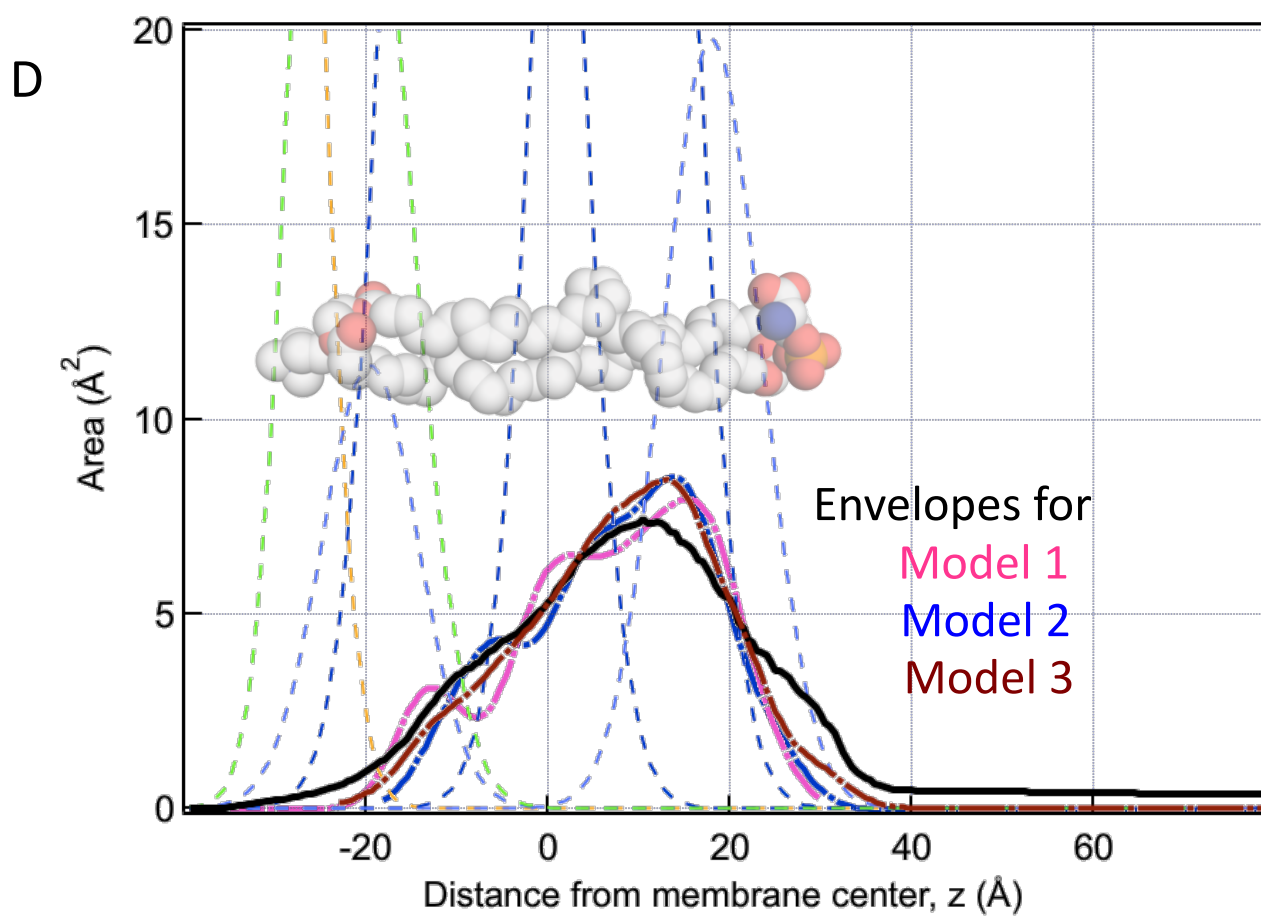
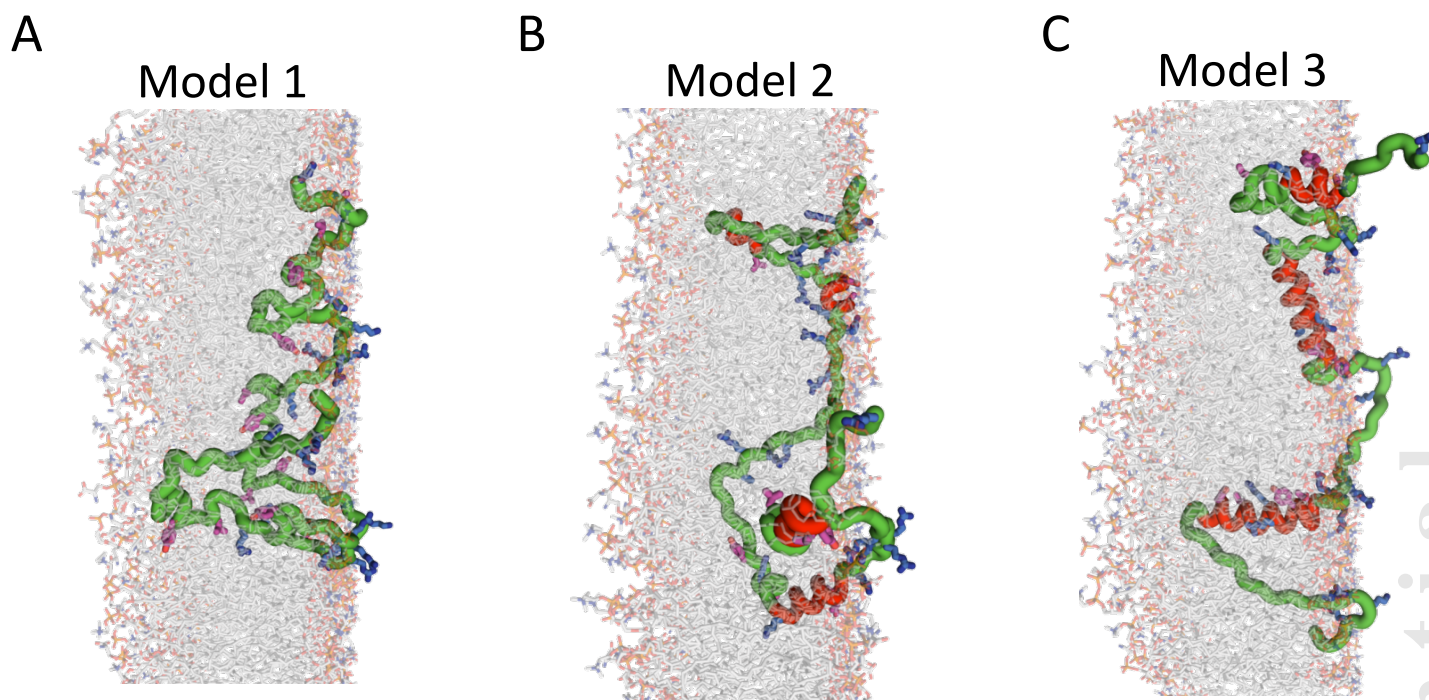
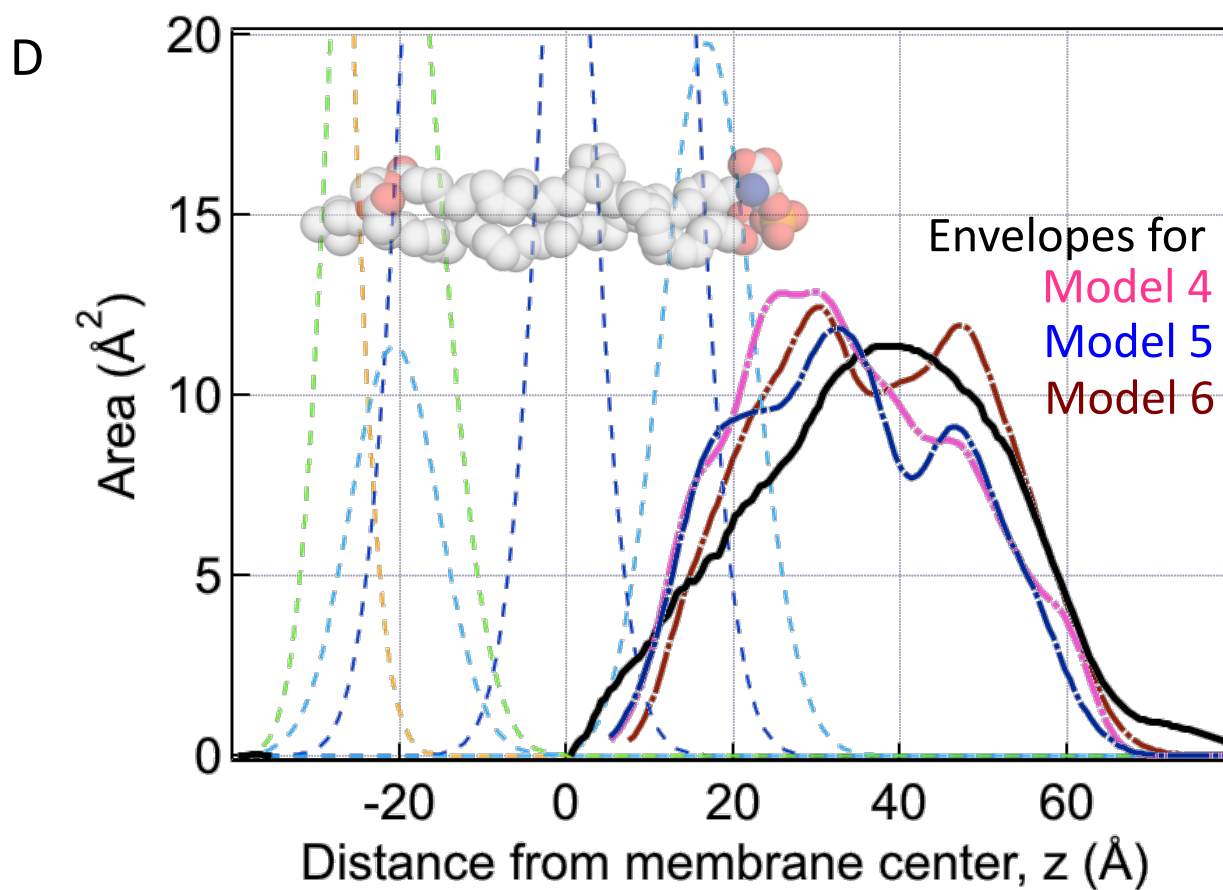
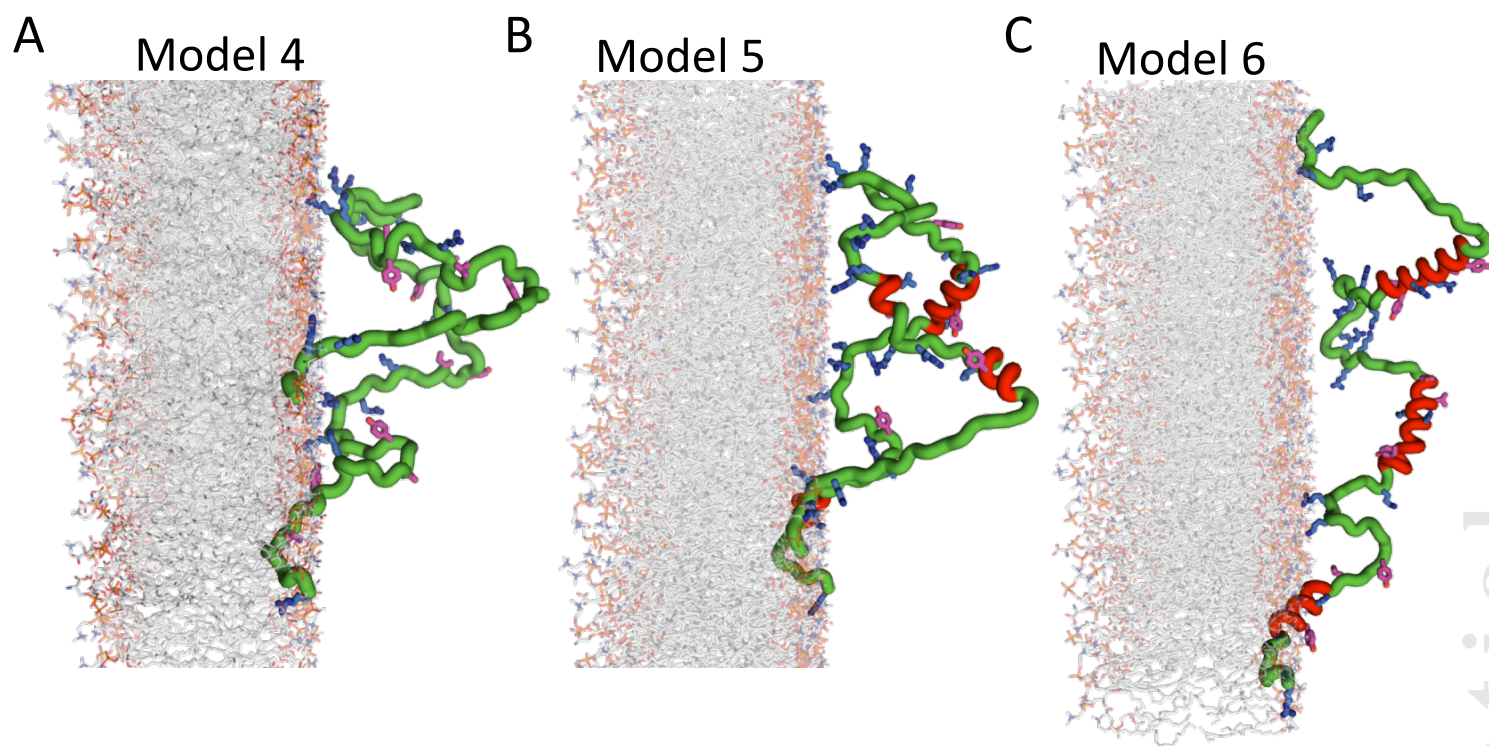


Figure 13



**The cytosolic domain of T-cell receptor  $\zeta$  associates with membranes in a dynamic equilibrium and deeply penetrates the bilayer**

Kerstin Zimmermann, Rebecca Eells, Frank Heinrich, Stefanie Rintoul, Brian Josey, Prabhanshu Shekhar, Mathias Lösche and Lawrence J Stern

*J. Biol. Chem.* published online September 11, 2017

---

Access the most updated version of this article at doi: [10.1074/jbc.M117.794370](https://doi.org/10.1074/jbc.M117.794370)

Alerts:

- [When this article is cited](#)
- [When a correction for this article is posted](#)

[Click here](#) to choose from all of JBC's e-mail alerts